Site-specific data-driven probabilistic wind field modeling for the wind-induced response prediction of cable-supported bridges

Aksel Fenerci[1], Ph.D., Department of Structural Engineering, Norwegian University of Science and Technology, Trondheim, Norway

Ole Øiseth, Ph.D., Department of Structural Engineering, Norwegian University of Science and Technology, Trondheim, Norway

Keywords: *suspension bridge, buffeting response, probabilistic turbulence model, turbulence characteristics, cross-spectral density*

Abstract

In this study, full-scale wind velocity measurements are conducted at eight locations on the Hardanger Bridge girder to investigate the possibility of a probabilistic representation of the turbulence field along the bridge span. Using appropriate assumptions, the two-dimensional turbulence field along the structure is reduced to six turbulence parameters, which are considered as correlated lognormally distributed random variables. The directionality and wind speed dependence of the parameters are demonstrated by means of wind roses and scatter diagrams. Depending on the wind speed and direction, simulations of the turbulence field were carried out using random number generators. The performance of simulated wind fields in capturing the variability and correlation structures of an actual wind field at a site is tested by detailed comparisons with the measurement data. For the sake of illustration, simulations were also performed for the design wind speed of the Hardanger Bridge using the current model and another model from the literature. The resulting probabilistic model is suitable for implementation in reliability-based frameworks and long-term extreme response analysis.

Introduction

There is an increasing global demand for long-span cable-supported bridges around the world, as the world population and urbanization grow rapidly. Although the nearly 20-year-old Akashi-Kaikyo suspension bridge still holds the world record for the longest span, during the last two decades a large number of long-span bridge projects were realized. The possibility of building super long-span suspension bridges (greater than 3000 m spans) has also been considered for long and deep straits such as the Gibraltar Strait or the Messina Strait. Recently, a similar effort was initiated by the Norwegian government (Dunham, 2016; Ellevset and Skorpa, 2011). As the span lengths of cable-supported bridges increase, wind-induced effects become of primary importance. In addition to potentially destructive phenomena such as flutter, the buffeting response of such structures is also critical and may govern design, especially for the serviceability and fatigue limit states (Xu, 2013). The buffeting response of cable-supported bridges have been analyzed using a stochastic dynamics framework (Davenport, 1962; Jain et al., 1996; Scanlan, 1978), which relies on an accurate description of the turbulent wind loads acting on the structure. This description is commonly achieved using the cross-spectral densities of the turbulence components, which are assumed to be zero-mean stationary Gaussian stochastic processes. Over the years, many spectral formulae have been suggested by researchers in this regard (Busch and Panofsky, 1968; Davenport, 1961; ESDU 086010, 2001; ESDU 85020, 2001; Kaimal et al., 1972; Krenk, 1996; Kristensen and Jensen, 1979; Mann, 2006; Simiu and Scanlan, 1996; Solari, 1987; Tieleman, 1995; Toriumi et al., 2000; von Karman, 1948). Most of the formulae are restricted to flat homogenous terrain and neutral atmospheric conditions. Several attempts have also been made for spectra in complex terrain (ESDU 85020, 2001; Mann, 2000; Nielsen et al., 2007; Panofsky et al., 1982; Tieleman, 1992).

[1] Corresponding author: aksel.fenerci@ntnu.no

In bridge design, such spectral formulae are commonly used. Regardless of the spectral form adopted, the spectral parameters are deterministic where the mean wind speed remains as the only design parameter. This approach ignores any uncertainty in turbulence parameters, which might arise due to the intrinsic random nature of the wind. However, Solari and Piccardo showed that the parameters of the turbulence spectra exhibited vast variability between measurements at different sites (Solari and Piccardo, 2001). The last couple of decades witnessed an impressive number of full-scale measurement campaigns focusing on wind characteristics (Bastos et al., 2018; Cao et al., 2009; Caracoglia and Jones, 2009; Cheynet et al., 2016; Cross et al., 2013; Höbbel et al., 2018; Hui et al., 2009a; Li et al., 2015; Liu et al., 2009; Miyata et al., 2002; Wang et al., 2013). The long-term measurements presented by researchers indicate large randomness in the wind characteristics. Remarkable scatter has also been reported in field measurement results of wind characteristics at specific bridge sites identified with complex terrain (Bastos et al., 2018; Cao et al., 2009; Fenerci et al., 2017; Hui et al., 2009b, 2009a). Moreover, in recent studies, it was also reported that this variability has implications on the buffeting response analysis of long-span cable-supported bridges and should not be ignored during the design (Fenerci et al., 2017; Fenerci and Øiseth, 2017).

Modern approaches to structural design and assessment suggest consideration of uncertainties in the structural and aerodynamic properties of structures, as well as in the environmental loading. The effect of these uncertainties on the dynamic response can be taken into account in previously established frameworks such as probabilistic response analysis (Kareem, 1988; Minciarelli et al., 2001; Solari, 1997), reliability analysis (Davenport, 1983a, 1983b; Kareem, 1987; Pagnini, 2010; Xu, 2013; Zhang et al., 2008) or performance-based design (Ciampoli et al., 2011; Spence and Kareem, 2014). In such analyses, a probabilistic turbulence model is often needed to propagate the parametric uncertainties due to the inherent variability of the wind turbulence field into the response estimates. A probabilistic model of this sort is also useful for the estimation of a long-term extreme response, when a full long-term approach is adopted (Giske et al., 2017; Xu et al., 2017). In an estimation of the long-term extreme response in this manner, a joint probability distribution of all parameters governing the turbulence field, such as turbulence intensities, integral length scales or parameters defining one-point and two point correlation structures of the turbulence, has to be defined (Naess and Moan, 2012; Xu et al., 2017). Thereby, with the available response analysis and design tools at hand, a good probabilistic description of the variable turbulence field at the considered site is needed.

Although the need for a probabilistic description of a wind field has been stressed extensively during the past years, little work has been performed towards development of such models. The only probabilistic model, to the authors' knowledge is of Solari and Piccardo (2001), which is based on a large amount of measurement data from different sites reported in the literature. Although its performance is yet to be tested, such a model includes the variability between the different sites and measurement campaigns, which might result in overly conservative uncertainty estimates for a specific site.

In the present study, a probabilistic description of the turbulence field along the Hardanger Bridge (HB) in Norway is carried out using long-term monitoring data. The turbulence spectra are modeled with simple expressions with only a few parameters, which are frequently used in practice. The probability distributions and correlation structure of the turbulence parameters, conditional on the mean wind speed and direction, are deduced using measurement data. Using a random number generator, simulations of the turbulent wind field are generated and compared with measurement data to assess the validity of the model. Finally, simulations for the design wind speed of the HB are conducted using both the current model and another model developed earlier by Solari and Piccardo.

Wind conditions at the Hardanger Bridge site

In Western Norway, the Hardanger Bridge (HB) crosses the Hardangerfjord and today it remains the longest suspension bridge in Norway with its main span of 1308 meters. The bridge is situated in a mountainous and complex terrain (Fig. 1) in the Norwegian fjords and is exposed to strong European windstorms. As part of a research project funded by the Norwegian Public Roads Administration (NPRA), wind velocities at several locations along the bridge girder have been monitored since December 2013 by the Norwegian University of Science and Technology (NTNU). Detailed information on the instrumentation and the workings of the monitoring system can be found in (Fenerci et al., 2017; Fenerci and Øiseth, 2017). The layout of the wind sensors on the bridge are shown schematically in (Fig. 2) and the coordinates of the sensors are given in Table 1. The monitoring system, which has been permanently installed on the bridge since 2013, records data in a discontinuous manner with a predefined trigger wind speed of 15 m/s. This means that a recording with a 30-minute duration is taken each time the trigger value is exceeded by a 1-minute mean speed in any of the anemometers. The system is also triggered manually from time to time in a random manner to include recordings with low mean speeds in the database and avoid excessive storage demand at the same time.

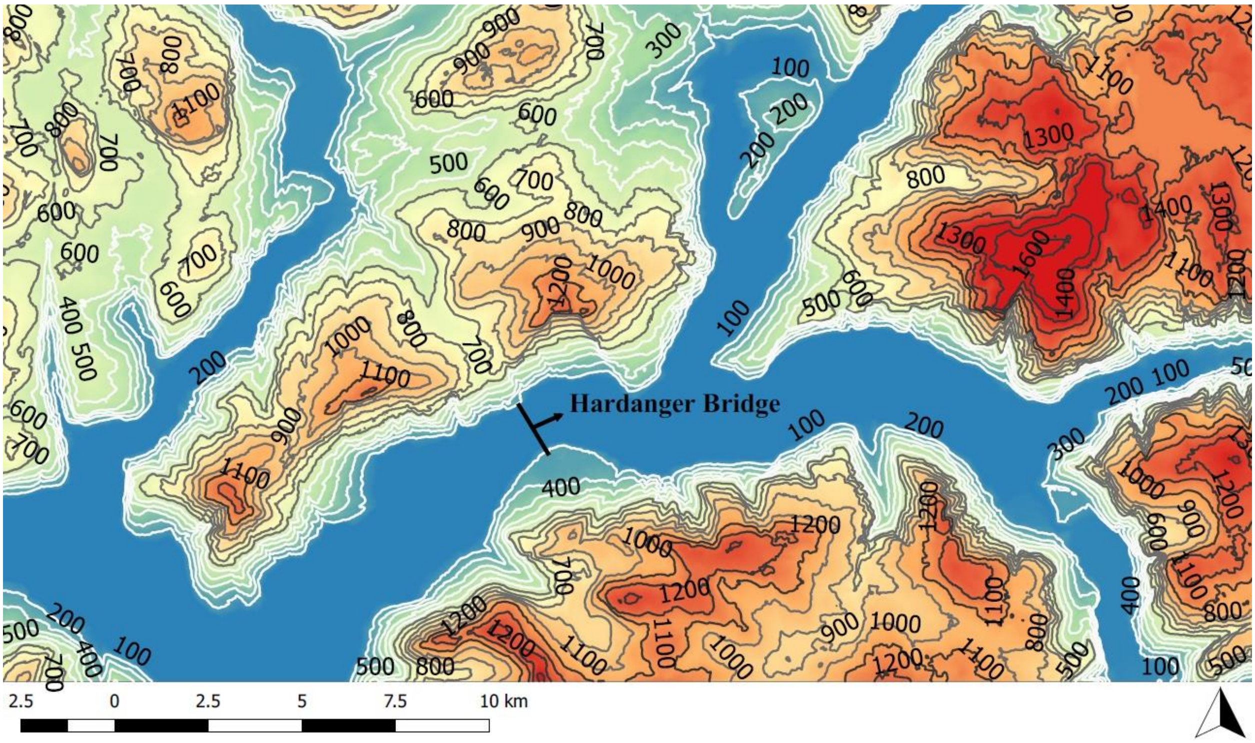

Fig. 1. Local topographical map of the Hardanger Bridge site

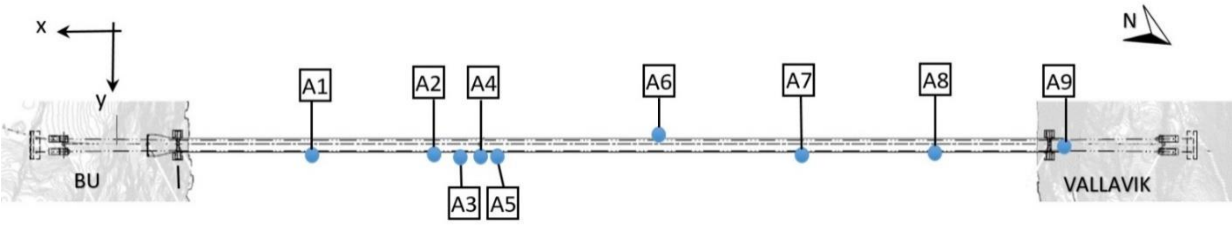

Fig. 2. Layout of the wind sensors

Table 1 Coordinates of the wind sensors (the origin of the coordinate system is the midspan of the bridge)

	A1	A2	A3	A4	A5	A6	A7	A8	A9
x (m)	460	280	240	200	180	-10	-180	-420	-655
y (m)	7.25	7.25	7.25	7.25	7.25	-7.25	7.25	7.25	4.5
z (m)	0.3	3.2	3.9	4.6	4.9	8	5.2	1.2	140

Then, the acquired wind velocity data from the anemometers are collected into a dataset to study the long-term wind characteristics, and an averaging interval of 10 minutes is adopted to obtain the turbulence statistics. This resulted in 15386 recordings with a 10-minute duration each in the dataset. The data quality is ensured and the data are adjusted for errors. The recordings with significant downtime or error values are discarded from the dataset. The wind velocity data were first recorded in polar coordinates and then decomposed into a mean (static) part in the horizontal plane and three fluctuating (turbulent) components. In a Cartesian coordinate system directed along the along-wind direction (mean wind direction), three orthogonal turbulence components were defined, namely, the along-wind (u), cross-wind (v) and vertical (w) turbulences. Using these turbulence components, three turbulence intensity components can be defined accordingly as

$$I_u = \frac{\sigma_u}{U}, I_v = \frac{\sigma_v}{U}, I_w = \frac{\sigma_w}{U} \tag{1}$$

where $\sigma_{u,v,w}$ denote the standard deviations of the three turbulence components and U denotes the mean wind speed. The turbulence intensity provides an elegant measure of the intensity of the wind speed fluctuations and is one of the most descriptive statistics of turbulence since it directly relates to the energy content of the turbulence.

For the 10-minute recordings in the dataset, using the data from the midspan sensor (A6) only, wind rose scatter plots of the mean wind speed and the three turbulence intensities are presented in Fig. 3 to provide an overview of the general wind conditions at the site. The recordings with mean wind speeds lower than 3 m/s were discarded from the data set. Due to high number of data points in the plots, the relative data density was calculated for a fine rectangular grid in the plotting area, and the relative density was assigned to each point by means of color-coding. It should be noted that the density for the easterly and westerly winds were calculated separately. This allows a visualization of how the data are distributed according to the upwind direction and along a particular direction. The distinct spreading of the mean wind speed was observed for the easterly and westerly winds. It is also noticed that the turbulence intensity is higher for the winds approaching from the mountain side on the north, whereas it is smaller for winds blowing along the fjord.

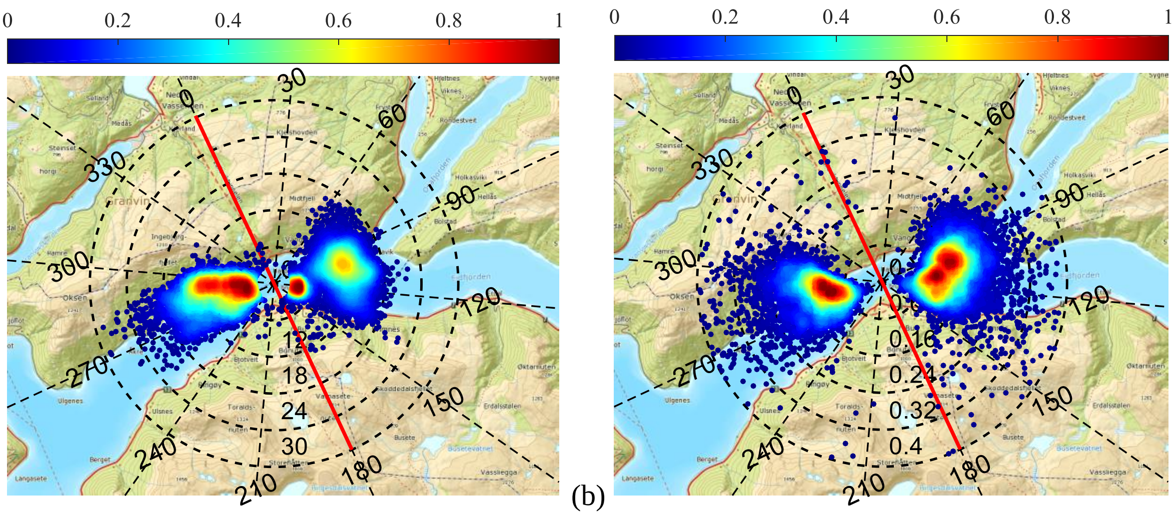

(a) (b)

(c) 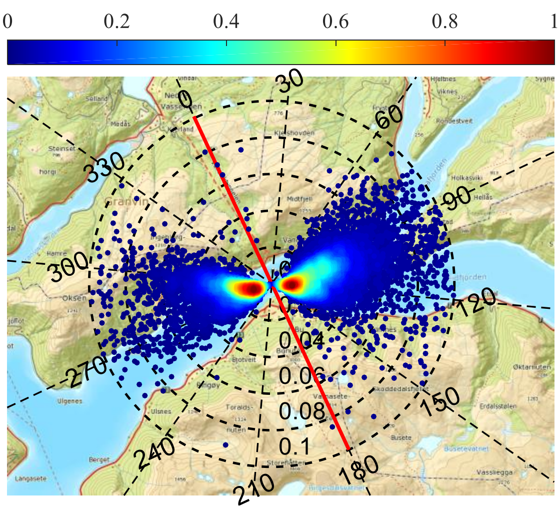

(d) 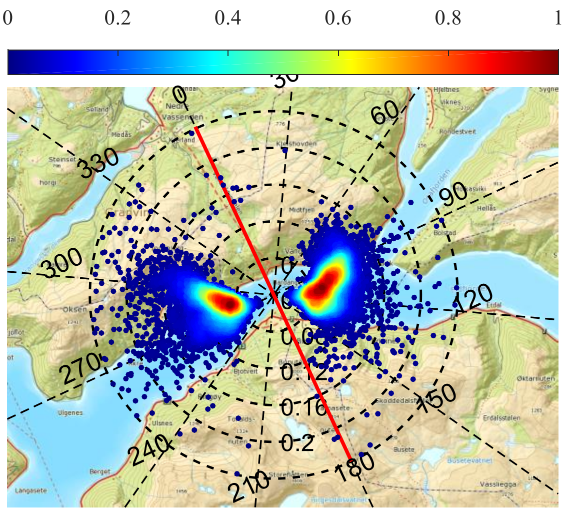

Fig. 3. Wind rose scatter plots: the (a) mean wind speed; (b) along-wind; (c) cross-wind and (d) vertical turbulence intensities at the midspan of the bridge (the color bar indicates the relative density of data points in the area, and red line highlights the bridge longitudinal axis)

Wind Field modeling

Modeling the relevant atmospheric turbulence field is of outmost importance in prediction of the wind-induced dynamic response of long-span bridges, since it is used to model the environmental dynamic loads acting on the structure. In the frequency domain, for a horizontal line-like structure, the turbulence field can be represented by a cross-spectral density tensor such as

$$S_{turb} = \begin{bmatrix} S_{uu}(\Delta x, f) & S_{uw}(\Delta x, f) \\ S_{wu}(\Delta x, f) & S_{ww}(\Delta x, f) \end{bmatrix} \tag{2}$$

Here, the cross terms are usually neglected since they have little influence on the dynamic response (Cheynet, 2016; Øiseth et al., 2013). The diagonal terms can be written as

$$\begin{aligned} S_{uu}(\Delta x, f) &= S_u(f) C_u(\Delta x, f) \\ S_{ww}(\Delta x, f) &= S_w(f) C_w(\Delta x, f) \end{aligned} \tag{3}$$

where $S_{u,w}(f)$ are the auto power spectral densities of the u and w turbulence components, $C_{u,w}$ are the normalized cross-spectral densities and f is the frequency. The normalized cross-spectra is a frequency dependent correlation coefficient, providing the spatial correlation of the turbulence components along the bridge longitudinal axis. For two points, x_1 and x_2, separated by a distance Δx, the normalized cross-spectra read

$$C_i(\Delta x, f) = \frac{S_i^{x_1 x_2}(\Delta x, f)}{\sqrt{S_i^{x_1}(f) S_i^{x_2}(f)}}, \quad i = u, w \tag{4}$$

where $S_{u,w}^{x_1 x_2}(\Delta x, f)$ are the cross-power spectral densities of the same turbulence component at points x_1 and x_2 separated by Δx. The cross-power spectral density has a real part and a complex part as usual, where the complex part contains phase information. In the case of separations in the horizontal plane perpendicular to the along-wind direction, the phase is usually small and often neglected (ESDU 086010, 2001; Simiu and Scanlan, 1996). The normalized spectra containing only the real part is also referred to as the normalized co-spectra. In summary, a modeling of the turbulence field for a horizontal line-like structure requires the definition of two auto-spectral densities and two normalized co-spectra for the u and w turbulence components.

The literature is rich on formulae for the spectral densities of the turbulence components, which were derived both on empirical and theoretical bases. However, most models rely on the assumption of a flat and homogenous terrain and neutral atmospheric stability. Moreover, the models are based on deterministic coefficients or simple variables as functions of the height above the ground or the roughness length, which makes it difficult to reflect the variability in the turbulence characteristics due to complex topographical effects. In previous papers by the authors (Fenerci and Øiseth, 2017, 2018), it was shown that the auto-spectra and normalized co-spectra of turbulence component at the HB site could be represented well with two simple expressions commonly used in the literature when the parameters of these expressions were fitted to the measured data. The expressions for the auto-spectra are of a Kaimal-type (Kaimal et al., 1972; Simiu and Scanlan, 1996), where the normalized co-spectra is of a Davenport type (Davenport, 1961), which read

$$\frac{S_{u\{w\}} f}{\sigma_{u\{w\}}} = \frac{A_{u\{w\}} f_z}{(1+1.5A_{u\{w\}} f_z)^{5/3}}, \quad f_z = \frac{fz}{U}$$
$$C_{u\{w\}} = \exp(-K_{u\{w\}} \frac{f \Delta x}{U}) \tag{5}$$

where z is the height above ground level (68 meters above sea level for the HB), which ensures dimensional consistency. The non-dimensional parameters $A_{u,w}$ and $K_{u,w}$ are to be fitted to the 10-minute measurements and are referred to as the spectral parameter and the decay coefficient, respectively. Adopting the above expressions, for a particular mean wind speed and direction, the turbulence field for the entire structure can be defined with just six parameters ($\sigma_{u,w}$, $A_{u,w}$, $K_{u,w}$), which can be treated as random variables. In sequence, these parameters relate to the energy content and correlation lengths of the turbulence components along the along-wind and bridge longitudinal axes. Nevertheless, to use these parameters in a probabilistic framework, an elaborate investigation of their underlying probability distributions, dependence on the mean wind speed or direction and correlation structures is needed.

Using the data from the midspan sensor (A6) the one-point statistics and the data from the closely spaced sensor pairs (A3-A4, A4-A5) for the two-point statistics, the six turbulence parameters were calculated for all 10-minute recordings above 3 m/s mean wind speed. The parameters are presented in Fig. 4 in terms of wind rose scatter plots using the same manner as in Fig. 3. The power spectral densities of the 10-minute signals were estimated using Welch's method of averaged periodograms (Welch, 1967), where 8 segments with 50% overlap were averaged to reduce the variance in the Fast Fourier Transform (FFT) estimates. The expressions of Eqn. (5) were then fitted to the estimated auto and normalized co-spectra of the turbulence components using a nonlinear least-squares approximation to obtain the $A_{u,w}$ and $K_{u,w}$ parameters. Observing the plots, the distinct distribution of data for the easterly and westerly winds and dependence of the parameters on the upwind direction are noted. A mountainous upwind terrain was associated with high turbulence ($\sigma_{u,w}$), where the spectral parameter $A_{u,w}$ was higher for the fjord exposure. The decay coefficient $K_{u,w}$ seems less sensitive to the wind direction, as it shows approximately uniform scatter with respect to the mean wind direction. Finally, the cross-correlation coefficient between the vertical and along-wind turbulence components are plotted in the same manner (Fig. 5). The cross-correlation coefficient, by definition, assumes values between -1 and 1, and it relates to the vertical shear or energy loss of turbulence due to ground roughness. It can be observed from Fig. 5 that it is in general positive at the HB site, which would not be expected for flat homogenous terrain. It is also apparent that the correlation is usually low, and the results are severely scattered. Considering the small effect of the correlation on the analytical prediction of the dynamic response and the severe scatter in data, the correlation between the two spectral components will be neglected.

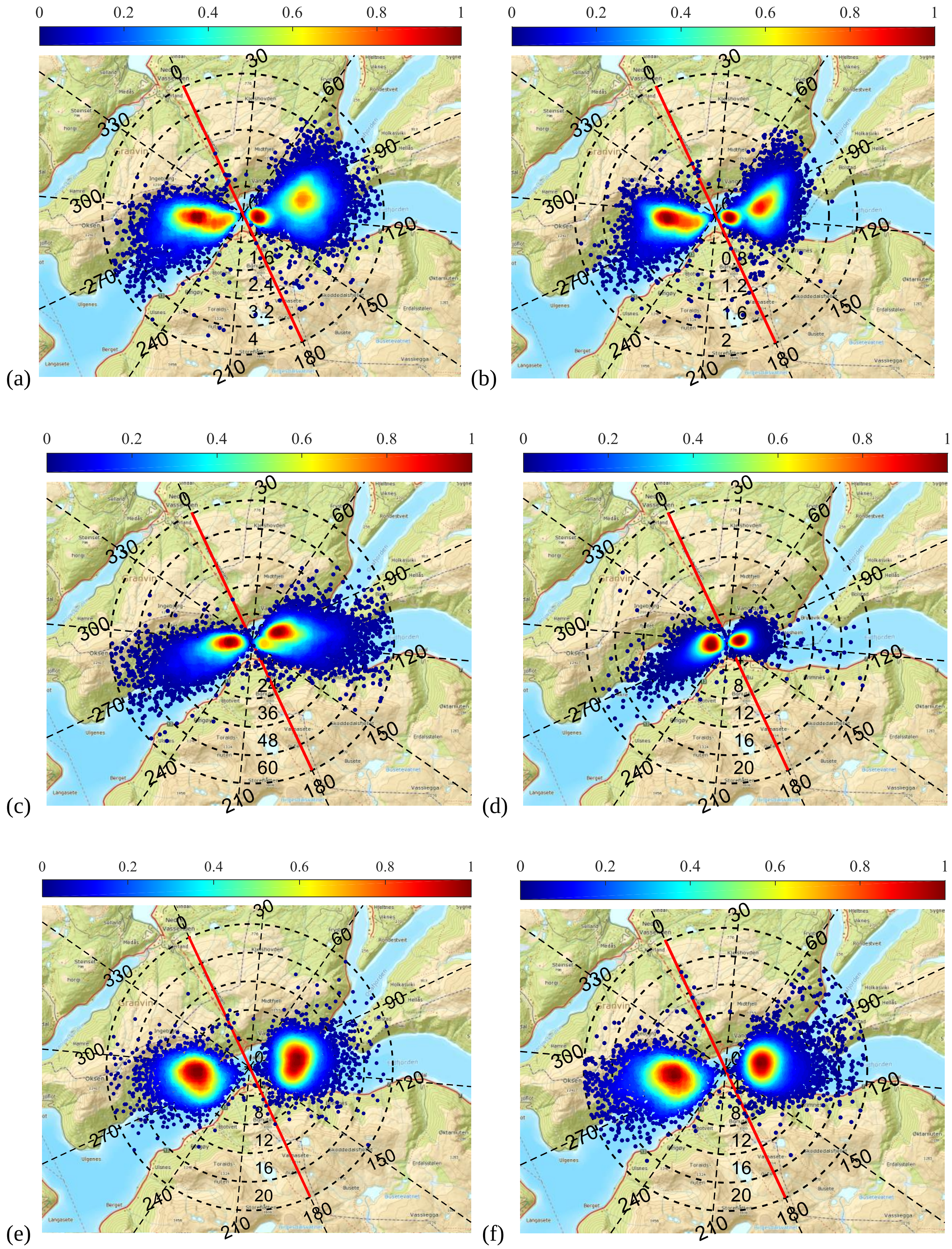

Fig. 4. Wind rose scatter plots of the turbulence parameters: (a) σ_u; (b) σ_w; (c) A_u; (d) A_w; (e) K_u and (f) K_w (the color bar indicates the relative data density; the red line indicates the bridge longitudinal axis)

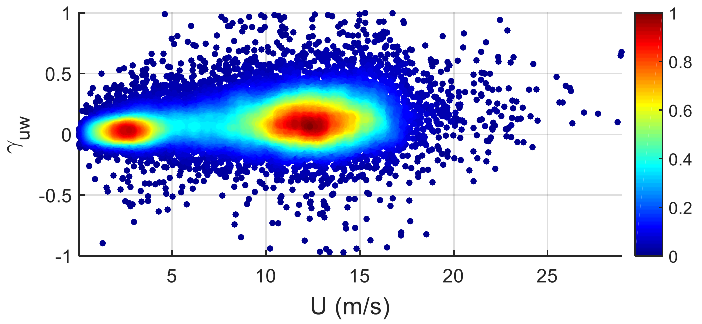

Fig. 5. Cross-correlation coefficient of along-wind and vertical turbulence components

In addition to the wind direction, it is deemed important to investigate the dependence of the turbulence parameters on the mean wind speed. Scatter plots are presented for each of the six parameters against the mean wind speed to reveal their dependence on the wind speed (Fig. 6 and Fig. 7). The data were plotted for the east and west winds separately. For each scatter diagram, the linear regression fits were plotted on top of the data to show the linear dependence on the variables. From the figures, a clear linear dependence was observed for the parameters σ_u, σ_w and A_u, where no significant dependence was detected for the three remaining parameters.

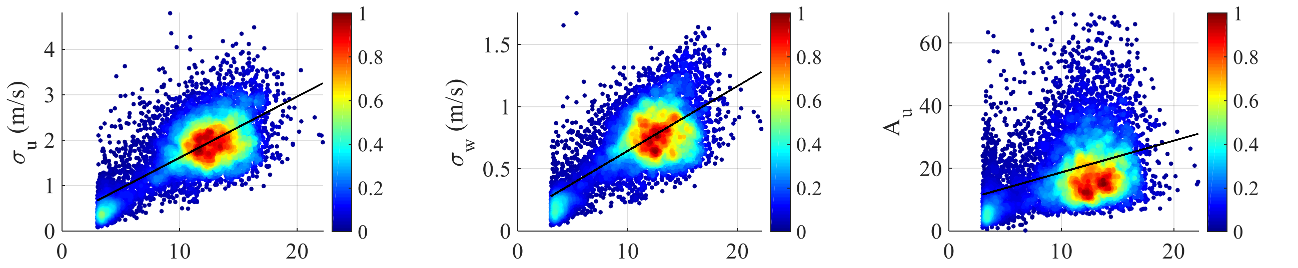

(a) (b) (c)

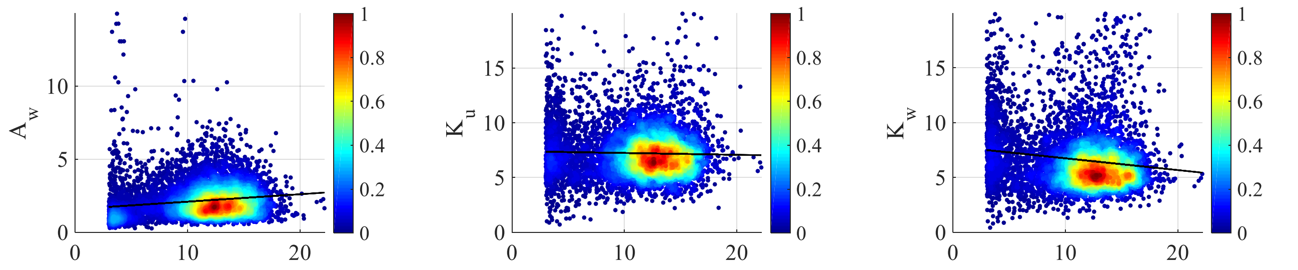

(d) (e) (f)

Fig. 6. Turbulence parameters against the mean wind speed for the easterly winds: (a) σ_u; (b) σ_w; (c) A_u; (d) A_w; (e) K_u and (f)K_w (the color bar shows the relative data density; the straight line is a linear regression fit)

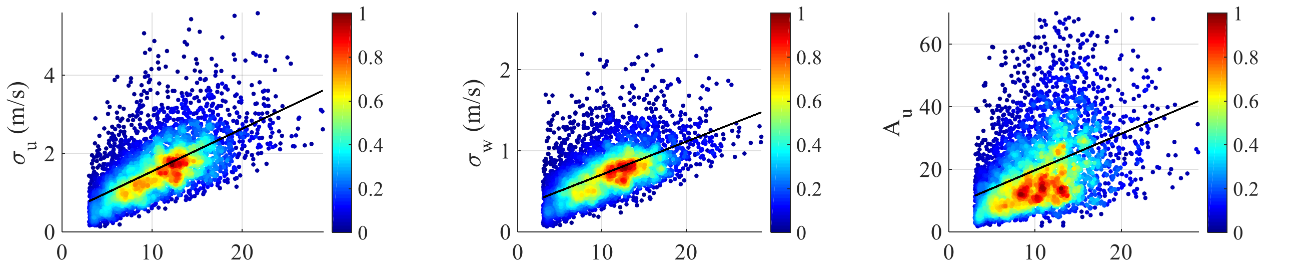

(a) (b) (c)

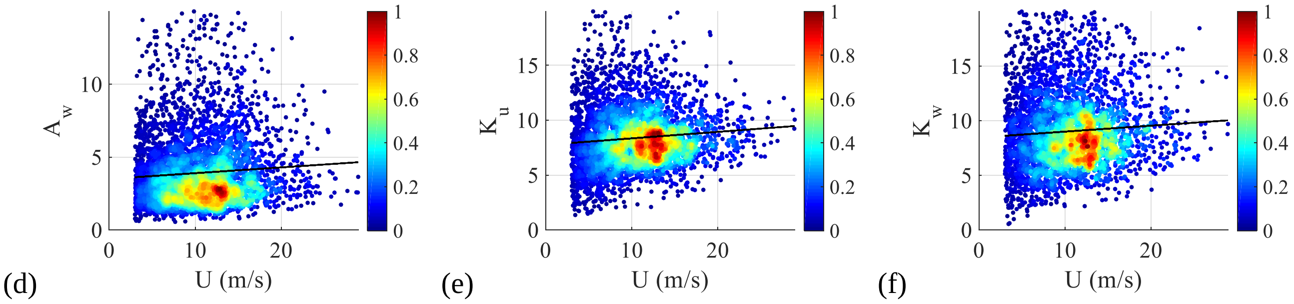

Fig. 7. Turbulence parameters against the mean wind speed for the westerly winds: (a) σ_u; (b) σ_w; (c) A_u; (d) A_w; (e) K_u and (f) K_w (the color bar shows the relative data density; the straight line is a linear regression fit)

Statistical properties of the turbulence parameters

Having established that the turbulence field at the HB site can be modeled with the six turbulence parameters dependent on the mean wind speed and the wind direction, their statistical properties, such as the underlying probability distributions and correlation structures, can now be established. To that extent, using all recordings with mean wind speeds above 10 m/s, the scatter diagrams of the six turbulence parameters were plotted against each other in a matrix form. The results are shown in Fig. 8 and Fig. 9 for the easterly and westerly winds, respectively. In the diagonal, histograms of the turbulence parameters are plotted, showing the probability density. The lognormal probability distributions were then fitted to the data and shown on top of the histograms. The probability density function (pdf) of the lognormal distribution can be written for a random variable x as

$$P(x \mid \tilde{\mu}, \tilde{\sigma}) = \frac{1}{x\tilde{\sigma}\sqrt{2\pi}} \exp\left(\frac{-(\ln x - \tilde{\mu})^2}{2\tilde{\sigma}^2} \right) \tag{6}$$

where $\tilde{\mu}$ and $\tilde{\sigma}$ are the parameters of the distribution, which are the mean and the standard deviation of the associated normal distribution, respectively. Note that for a lognormal distributed random variable x, the natural logarithm of x is normally distributed with the mean $\tilde{\mu}$ and the standard deviation $\tilde{\sigma}$. Therefore, the parameters of the lognormal distribution can simply be estimated by calculating the mean and the standard deviation of the natural logarithm of the random variable from available data. The lognormal distribution parameters are given in Table 2. From visual inspection, it is clear that the data are represented well with such probability distributions. Moreover, hypothesis testing (chi-square goodness of fit tests) are employed and the lognormal distributions are found appropriate at a 5% significance level. In the off-diagonals, scatter plots of turbulence parameters were plotted against each other, showing their correlation structures. Linear regression curves were also plotted along with the scatter diagrams to highlight the trends present in the plots, which are not apparent due to the large number of data points and large scatter. A strong linear dependence between the turbulence standard deviations σ_u and σ_w is immediately evident after a first look at the matrix plots. For the easterly and westerly winds, the matrices of the correlation coefficients of the turbulence parameters are tabulated in Table 3. Examining the table and the scatter diagrams, the correlations between σ_u and σ_w, A_u and A_w, K_u and K_w, σ_u and A_u and σ_w and A_w are considered significant, where the other pairs are assumed as uncorrelated. Note that different correlation structures are observed for the winds from two directions.

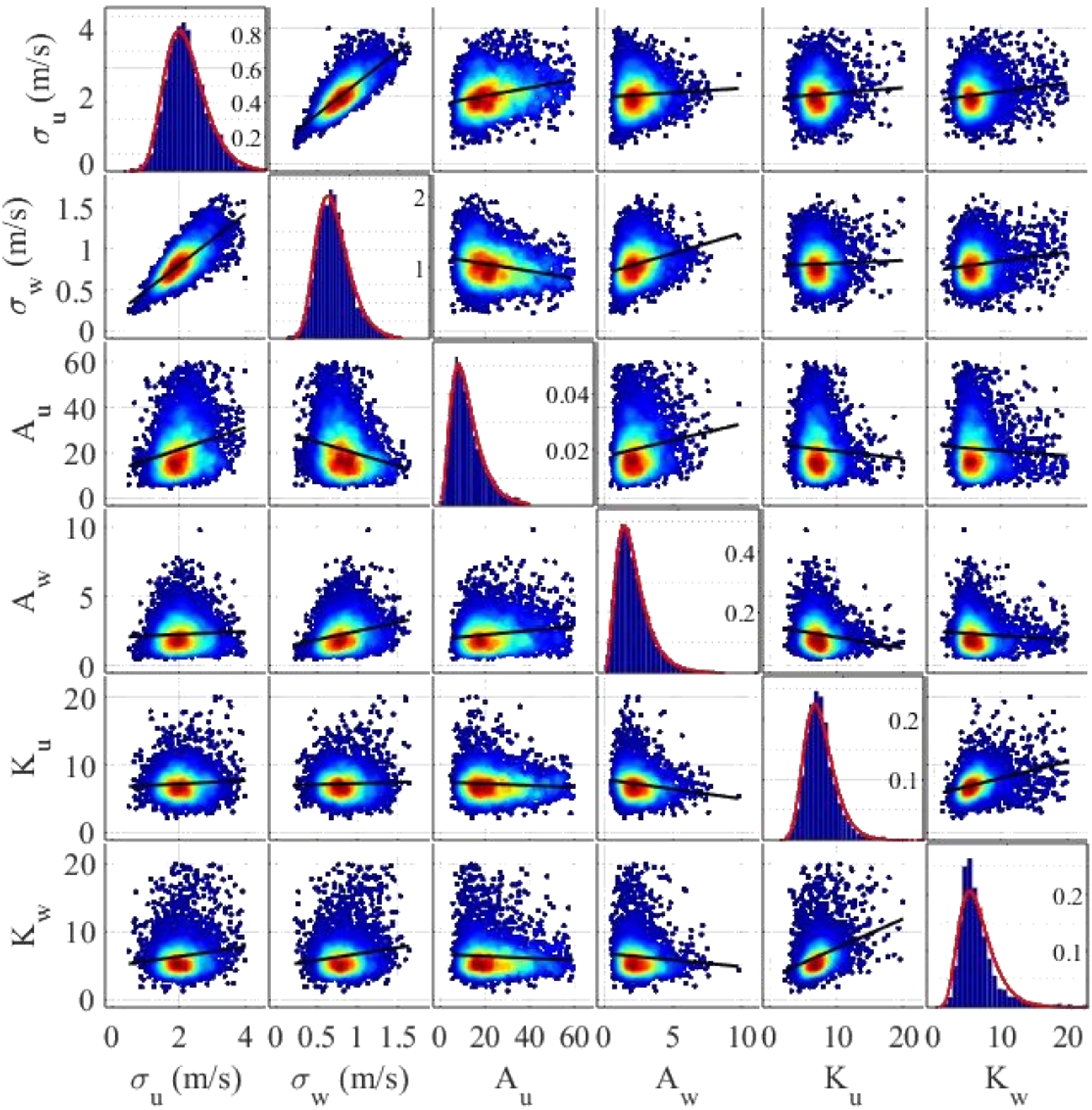

Fig. 8. The scatter plot matrix of the turbulence parameters for the easterly winds (the y-axis for the histograms indicating the probability density is shown on the right side of the plotting area)

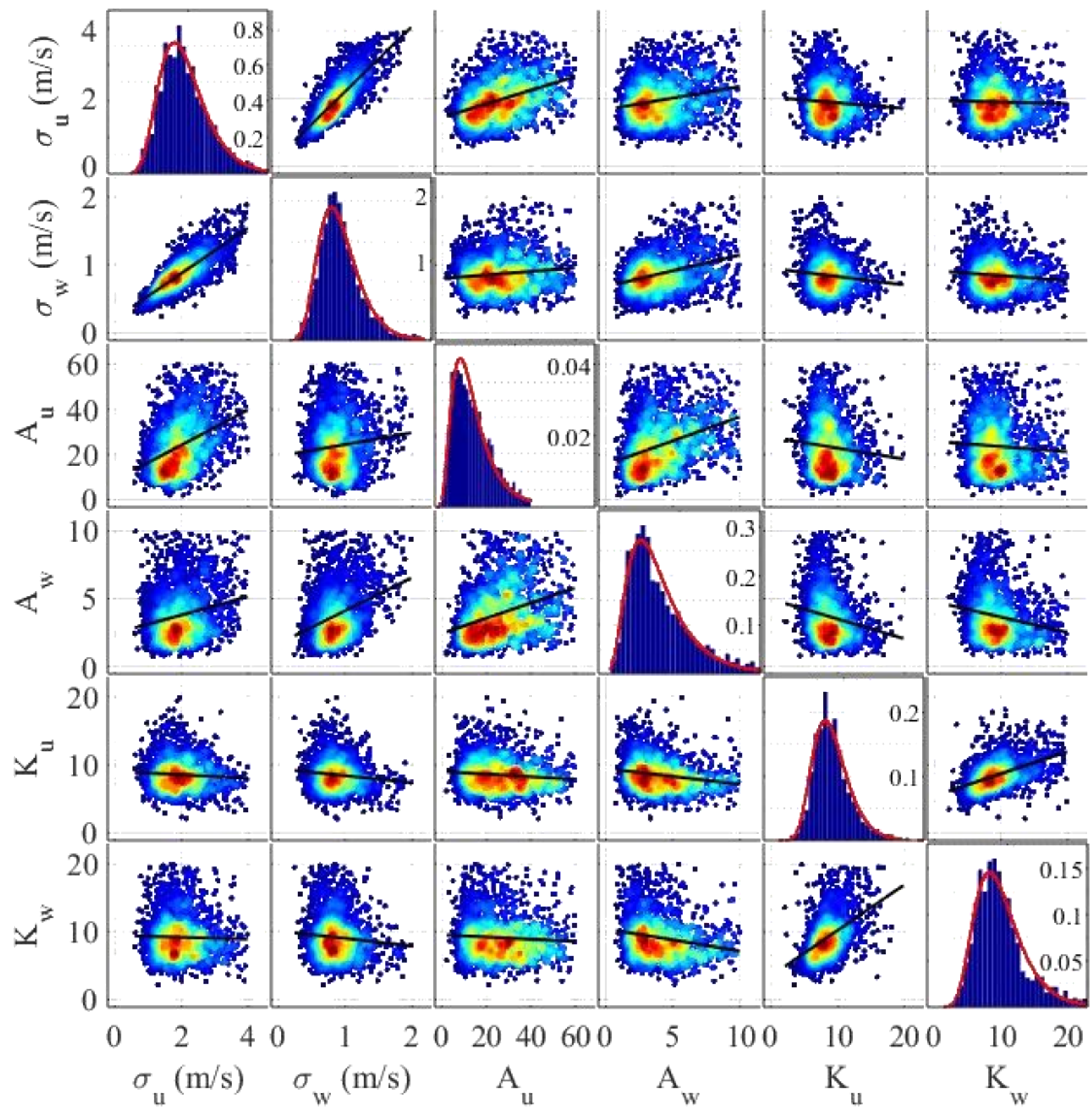

Fig. 9. The scatter plot matrix of the turbulence parameters for the westerly winds (the y-axis for the histograms indicating the probability density is shown on the right side of the plotting area)

Table 2 Lognormal distribution parameters for the easterly and westerly winds

		σ_u	σ_w	A_u	A_w	K_u	K_w
EAST	$\tilde{\mu}$	0.6753	-0.2468	2.9669	0.7076	1.9385	1.7932
	$\tilde{\sigma}$	0.2566	0.2632	0.4538	0.4466	0.2652	0.3423
WEST	$\tilde{\mu}$	0.6104	-0.1932	3.0364	1.2075	2.1093	2.1633
	$\tilde{\sigma}$	0.3159	0.3021	0.5282	0.4943	0.268	0.3322

Table 3 Correlation coefficients matrix for the easterly and westerly winds

		σ_u	σ_w	A_u	A_w	K_u	K_w
	σ_u	1	0.7608	0.2641	0.045	0.0458	0.1289
	σ_w	0.7608	1	-0.2056	0.2571	0.0044	0.1338
	A_u	0.2641	-0.2056	1	0.1633	-0.0678	-0.0564
	A_w	0.045	0.2571	0.1633	1	-0.1706	-0.0843
	K_u	0.0458	0.0044	-0.0678	-0.1706	1	0.3261
EAST	K_w	0.1289	0.1338	-0.0564	-0.0843	0.3261	1
	σ_u	1	0.8148	0.4087	0.1712	-0.0559	-0.0199
	σ_w	0.8148	1	0.053	0.2851	-0.1036	-0.0656
	A_u	0.4087	0.053	1	0.3065	-0.0525	-0.0385
	A_w	0.1712	0.2851	0.3065	1	-0.2059	-0.2002
	K_u	-0.0559	-0.1036	-0.0525	-0.2059	1	0.4725
WEST	K_w	-0.0199	-0.0656	-0.0385	-0.2002	0.4725	1

It was previously stated that some of the parameters (σ_u, σ_w, A_u) were also dependent on the mean wind speed (Fig. 6 and Fig. 7). Consequently, the probability distributions given in Fig. 8 and Fig. 9 and the corresponding lognormal distributions parameters given in Table 2 do not represent the true distribution of these parameters, since the dataset is not complete in the entire wind speed range. To overcome this problem and obtain a true statistical representation of these parameters, the probability distributions of these parameters should be established conditional to the mean wind speed. Accordingly, the data were divided into 1 m/s intervals, and the corresponding lognormal parameters were calculated for each interval. In each interval, a minimum number of 70 recordings were sought because the distribution is not apparent otherwise. Again, it is ensured that the sampled data comes from a lognormal distribution by hypothesis testing at a 5% significance level. The estimated lognormal distribution parameters and the correlation coefficients were then plotted against the mean wind speed (c). It is found that the parameters $\tilde{\mu}_{\sigma_u}$, $\tilde{\mu}_{\sigma_w}$ and $\tilde{\mu}_{A_u}$ linearly vary with the mean wind speed, where the remaining $\tilde{\mu}$ and $\tilde{\sigma}$ parameters and the correlation coefficients ρ remain constant. It is also seen that the behavior of the statistical parameters stabilize after the mean wind speed exceeds 10 m/s. This is thought to arise due to the nonstationarity of the signals below 10 m/s, where trends in the wind speed and rapid changes in the wind direction are common. Therefore, the linear curves were fitted to the estimates of $\tilde{\mu}_{\sigma_u}$, $\tilde{\mu}_{\sigma_w}$ and $\tilde{\mu}_{A_u}$ in the range above 10 m/s to model the conditional distributions of these parameters. For the others, average of values above 10 m/s were taken. A summary of the results is shown in Table 4.

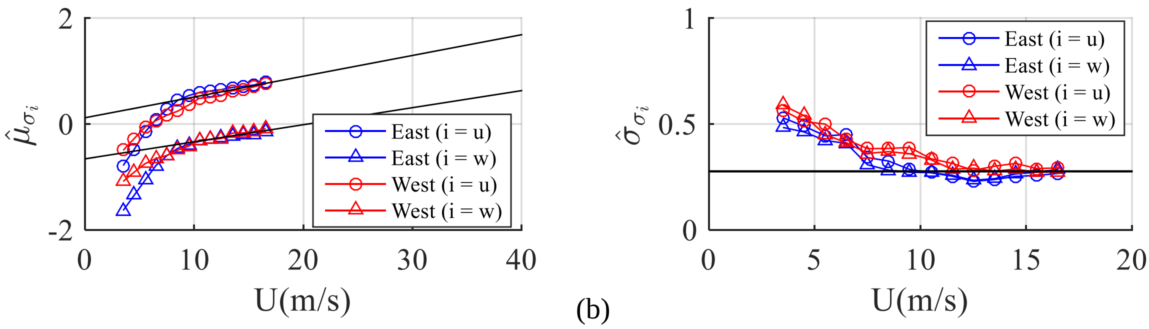

(a) (b)

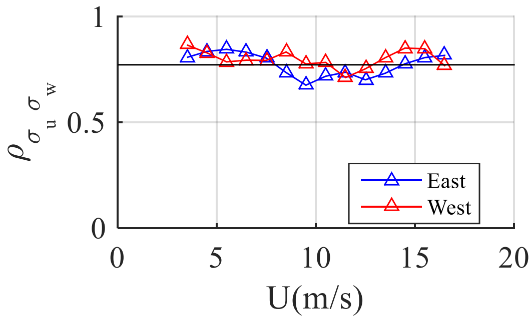

(c)

Fig. 10. Statistical parameters for the turbulence standard deviations: the (a) lognormal parameter $\tilde{\mu}$; (b) lognormal parameter $\tilde{\sigma}$ and (c) correlation coefficient ρ

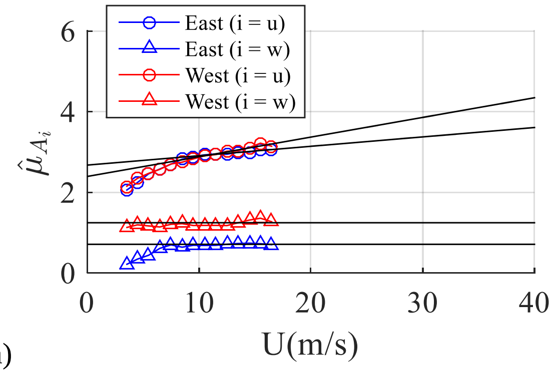

(a)

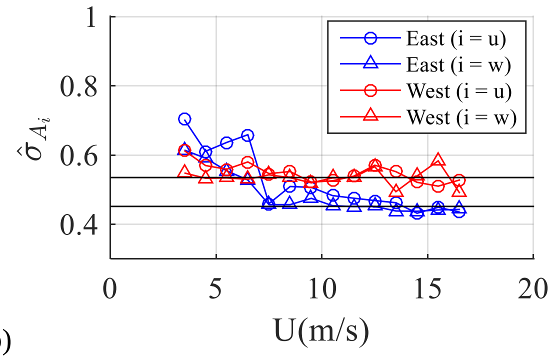

(b)

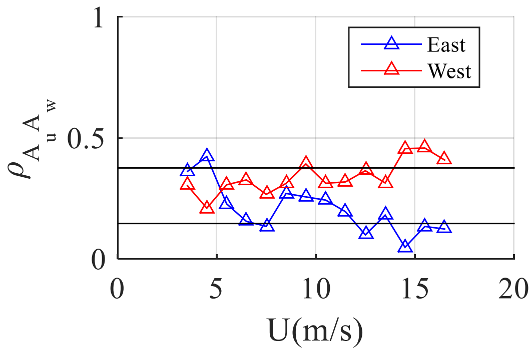

(c)

Fig. 11. Statistical parameters for the spectral parameter A: the (a) lognormal parameter $\tilde{\mu}$; (b) lognormal parameter $\tilde{\sigma}$ and (c) correlation coefficient ρ

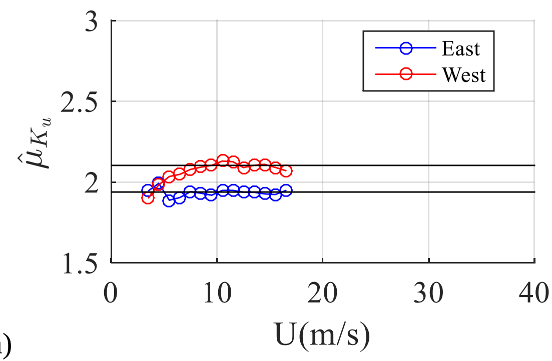

(a)

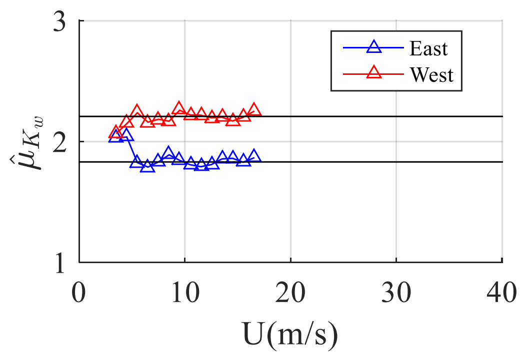

(b)

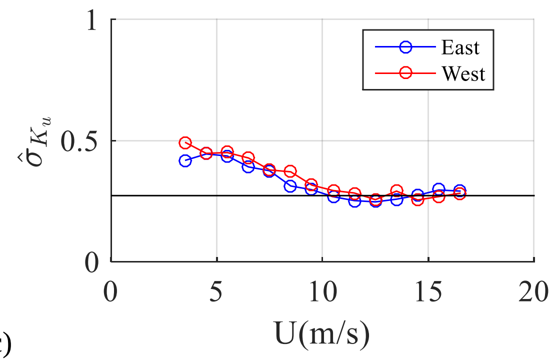

(c)

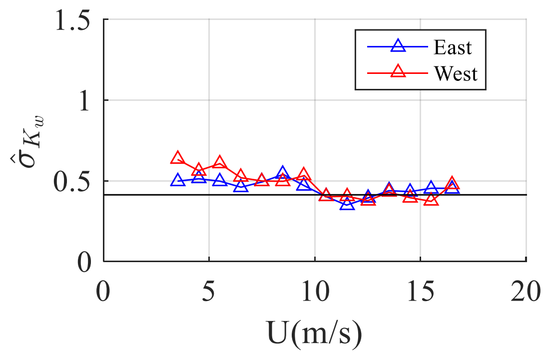

(d)

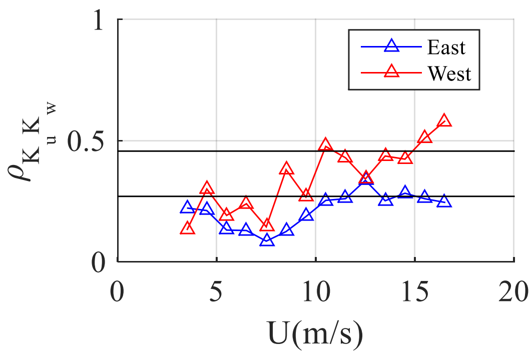

(e)

Fig. 12. Statistical parameters for the decay coefficient K: the (a) lognormal parameter $\tilde{\mu}_{K_u}$; (b) lognormal parameter $\tilde{\mu}_{K_w}$; (c) lognormal parameter $\tilde{\sigma}_{K_u}$; (d) lognormal parameter $\tilde{\sigma}_{K_u}$ and (e) correlation coefficient ρ

Table 4 Statistical properties of the turbulence parameters conditional to mean wind speed

	East			West		
	$\tilde{\mu}$	$\tilde{\sigma}$	ρ	$\tilde{\mu}$	$\tilde{\sigma}$	ρ
σ_u	0.122+0.039U	0.28	0.754	0.122+0.039U	0.28	0.772
σ_w	-0.657+0.032U	0.278		-0.657+0.032U	0.278	
A_u	2.67+0.0248U	0.456	0.15	2.407+0.048U	0.556	0.327
A_w	0.725	0.456		1.247	0.556	
K_u	1.938	0.275	0.267	2.11	0.275	0.459
K_w	1.833	0.415		2.213	0.415	

Ultimately, it was found appropriate to model $\tilde{\mu}_{\sigma_u}, \tilde{\mu}_{\sigma_w}$ and $\tilde{\mu}_{A_u}$ as functions of the mean wind speed and all the remaining parameters as constants. For an estimation of the constant parameters, all the data above a 10 m/s mean wind speed was used, as displayed in Table 2. The final lognormal distribution parameters and the correlation coefficient matrix are summarized in Table 5 and Table 6, respectively. As can be observed in Fig. 10-Fig. 12, the number of data points in the high wind speed range is rather limited and accordingly, the parameters were fitted using the data in the moderate wind speed range. Therefore, to show that the observations in the high wind speed range agrees with the distributions, they are plotted along the probability densities and showed in Fig. 13Fig. 15.

Table 5 Final lognormal parameters

		σ_u	σ_w	A_u	A_w	K_u	K_w
	$\tilde{\mu}$	0.122+0.039U	-0.657+0.032U	2.67+0.0248U	0.7076	1.9385	1.7932
EAST	$\tilde{\sigma}$	0.2566	0.2632	0.4538	0.4466	0.2652	0.3423
	$\tilde{\mu}$	0.122+0.039U	-0.657+0.032U	2.407+0.048U	1.2075	2.1093	2.1633
WEST	$\tilde{\sigma}$	0.3159	0.3021	0.5282	0.4943	0.268	0.3322

Table 6 Final correlation matrix

		σ_u	σ_w	A_u	A_w	K_u	K_w
	σ_u	1	0.7608	0.2641	0	0	0
	σ_w	0.7608	1	0	0.2571	0	0
	A_u	0.2641	0	1	0.1633	0	0
	A_w	0	0.2571	0.1633	1	0	0
	K_u	0	0	0	0	1	0.3261
EAST	K_w	0	0	0	0	0.3261	1
	σ_u	1	0.8148	0.4087	0	0	0
	σ_w	0.8148	1	0	0.2851	0	0
	A_u	0.4087	0	1	0.3065	0	0
	A_w	0	0.2851	0.3065	1	0	0
	K_u	0	0	0	0	1	0.4725
WEST	K_w	0	0	0	0	0.4725	1

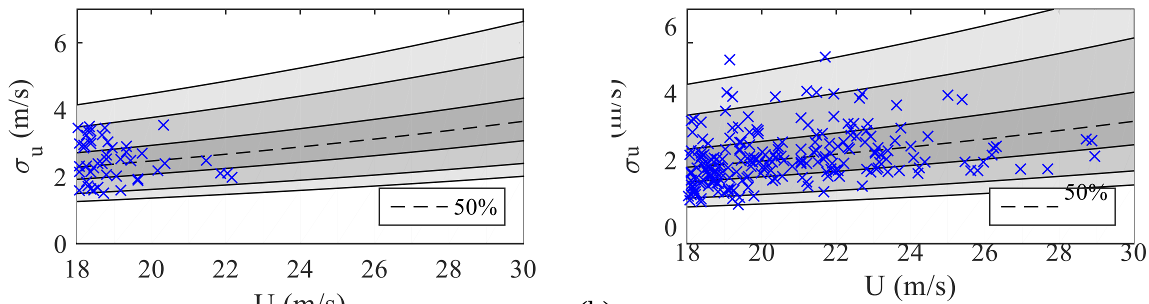

(a) (b)

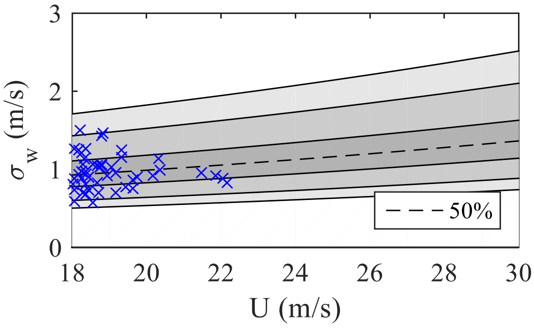

(c)
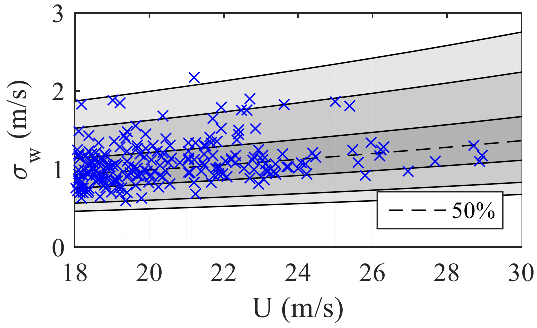

(d)

Fig. 13. Evolution of the probability distributions of the turbulence standard deviations: (a) σ_u–East (b) σ_u–West (c) σ_w–West and (d) σ_w–West (the continuous curves show the 1, 5, 25, 75, 95 and 99 percentiles of the distribution in order)

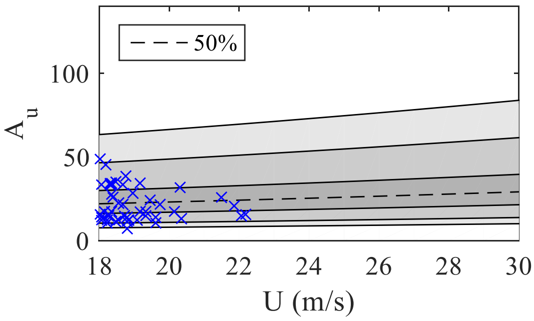

(a)
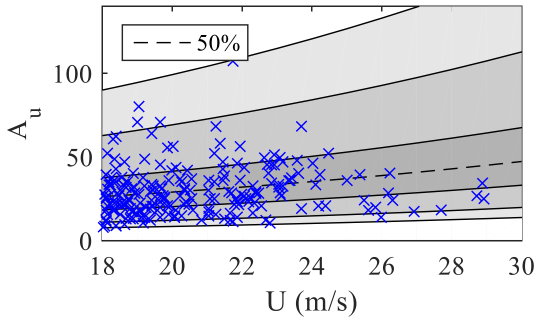

(b)

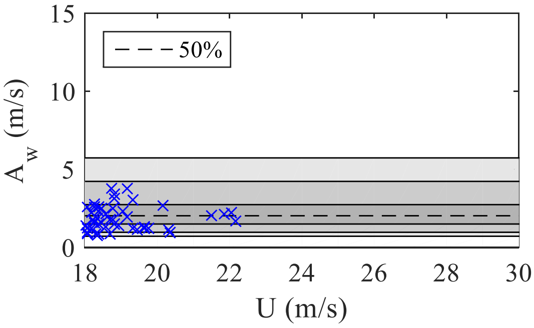

(c)
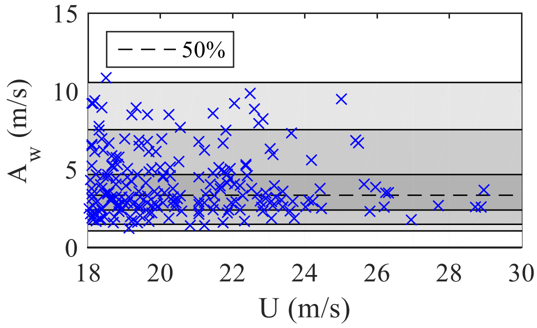

(d)

Fig. 14. Evolution of the probability distributions of the spectral parameters: (a) A_u–East; (b) A_u–West; (c) A_w–West and (d) A_w–West (the continuous curves show the 1, 5, 25, 75, 95 and 99 percentiles of the distribution in order)

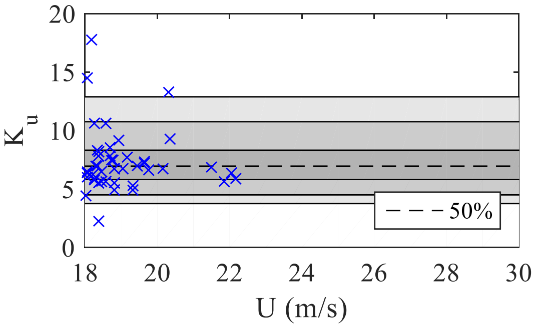

(a)
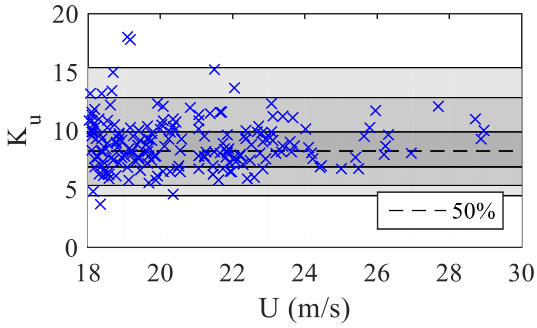

(b)

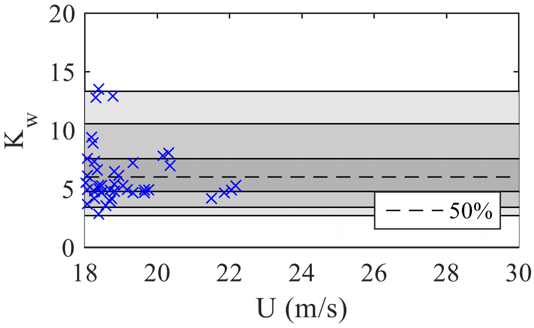

(c)

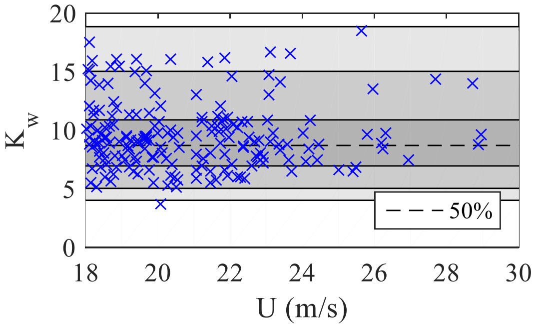

(d)

Fig. 15. Evolution of the probability distributions of the decay coefficients: (a) K_u–East; (b) K_u–West; (c) K_w–West and (d) K_w–West (the continuous curves show the 1, 5, 25, 75, 95 and 99 percentiles of the distribution in order)

Simulations of random wind fields

A probabilistic turbulence field was formulated in the previous section that consisted of six correlated and lognormally distributed random variables. This model was validated by comparing the simulations from the model with the measured data. For this purpose, correlated lognormally distributed random parameters were generated. Parameter generation was achieved using a standard normally distributed number generator (The Mathworks Inc., 2015) and then taking their exponent. Given the vector of lognormally distributed random variables

$$Y = \begin{bmatrix} \sigma_u & \sigma_w & A_u & A_w & K_u & K_w \end{bmatrix} \tag{7}$$

the natural logarithm of the elements of Y forms a vector of normally distributed random variables

$$X = \ln(Y) \tag{8}$$

The mean values and standard deviations of the elements of the vectors Y and X are denoted as (m_i, v_i) and $(\tilde{\mu}_i, \tilde{\sigma}_i),\ i = 1..6$, respectively, where the latter pair also represents the lognormal distribution parameters, as mentioned earlier. The two sets of statistical moments are related to each other as

$$\begin{aligned} m &= \exp(\tilde{\mu} + \tilde{\sigma}^2 / 2) \\ v &= \sqrt{\left(\exp(\tilde{\sigma}^2) - 1\right)\exp(2\tilde{\mu} + \tilde{\sigma}^2)} \end{aligned} \tag{9}$$

The covariance matrix of vector X can be written in terms of the covariance matrix of Y using (Zerovnik et al., 2012)

$$\operatorname{cov}(X_i, X_j) = \ln\left[\frac{\operatorname{cov}(Y_i, Y_j)}{m_i m_j} + 1\right],\ i = 1..6,\ j = 1..6 \tag{10}$$

which can be rewritten in terms of the correlation coefficient matrix of vector Y (ρ_y) and the vector $\tilde{\sigma}$ as

$$\operatorname{cov}(X_i, X_j) = \ln\left[(\rho_y)_{ij}\sqrt{\exp(\tilde{\sigma}_i^{\,2} - 1)}\sqrt{\exp(\tilde{\sigma}_j^{\,2} - 1)} + 1\right],\ i = 1..6,\ j = 1..6 \tag{11}$$

Using Eqn. (11), the covariance matrix of the vector X of the normally distributed random variables can be calculated. Using this covariance matrix and knowing the mean value vector $\tilde{\mu}$, a set of multivariate correlated normally distributed random variables can be obtained. Then, the corresponding lognormal random variables can obtained by taking their natural exponents.

Using above formulations along with the vectors of $\tilde{\mu}$, $\tilde{\sigma}$ given in Table 5 and the correlation coefficient matrix ρ given in Table 6, the random turbulence fields were generated for each 10 minute recording in the dataset. The conditional distributions for each simulation were established according to the mean wind speed and direction (east or west) of each individual recording. The simulated turbulence parameters were then compared with the measurement data in terms of scatter plots. The scatter plots with both measured and simulated turbulence components are shown in Fig. 16 and Fig. 18, respectively, for different mean wind velocity intervals. A brief look at the plots suggest that the target variability of the data is matched reasonably well by the simulations.

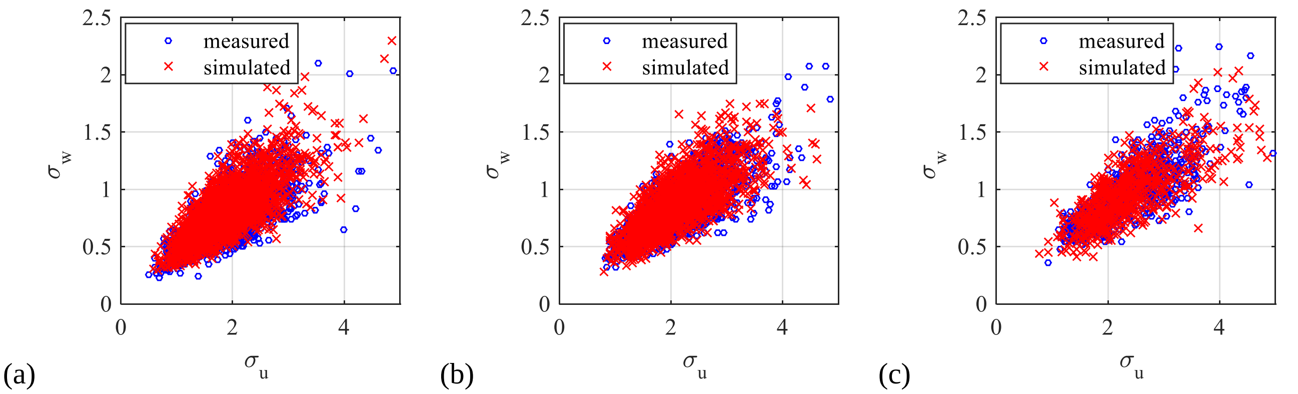

Fig. 16. Scatter plots of the measured and simulated turbulence standard deviations: (a) 10 ≤ U < 13 m/s; (b) 13 ≤ U < 16 m/s and (c) U ≥ 16 m/s

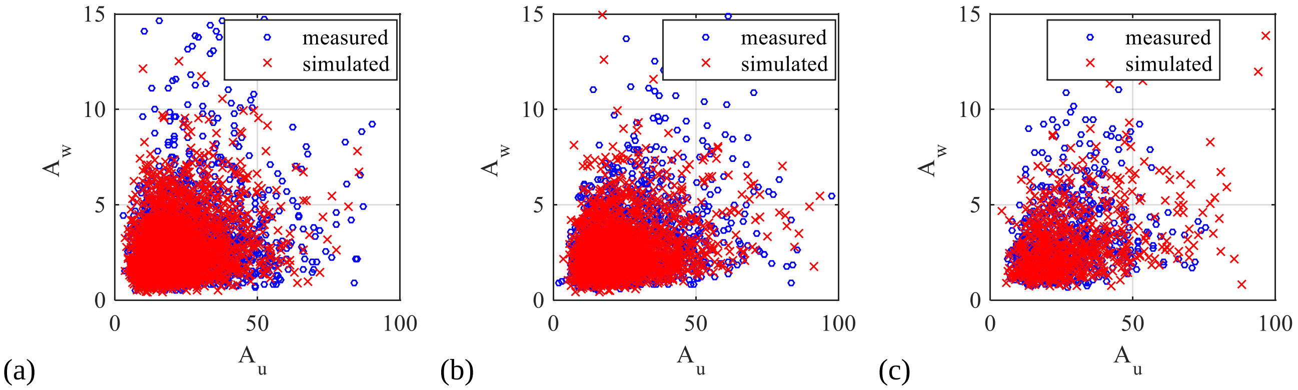

Fig. 17. Scatter plots of the measured and simulated turbulence spectral parameters: (a) 10 ≤ U < 13 m/s; (b) 13 ≤ U < 16 m/s and (c) U ≥ 16 m/s

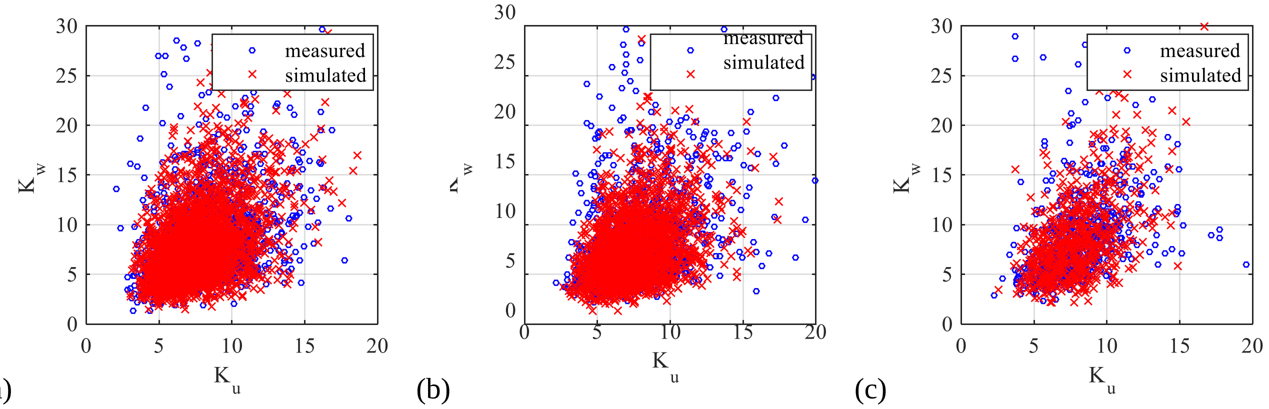

Fig. 18. Scatter plots of the measured and simulated decay coefficients: (a) $10 \leq U < 13$ m/s; (b) $13 \leq U < 16$ m/s and (c) $U \geq 16$ m/s

To have a more detailed look at the simulated wind field data and their correspondence with the measurements, the auto-spectral density and normalized co-spectra of the u and w turbulence, which are more familiar to engineers, are presented in Fig. 19 and Fig. 22, respectively. Only recordings with mean wind speeds above 10 m/s were considered. The simulated and measured spectra display a reasonable agreement. The relative data density is once again shown using color-coded data points. It is observed that for a given frequency, the auto-spectral density also follows a lognormal distribution. Fitting the lognormal distributions to the measured and simulated data, the peak of the distribution (mode) and the 95 percentile values for the auto-spectra were obtained and included in the same figures. These are obtained by fitting a lognormal probability distribution to the spectra at each discrete frequency. For a clearer comparison, the measured and simulated auto-spectra were plotted on top of each other, as shown in Fig. 23. Excellent agreement is observed between the percentile values, implying that the simulations are statistically representative of the measurements.

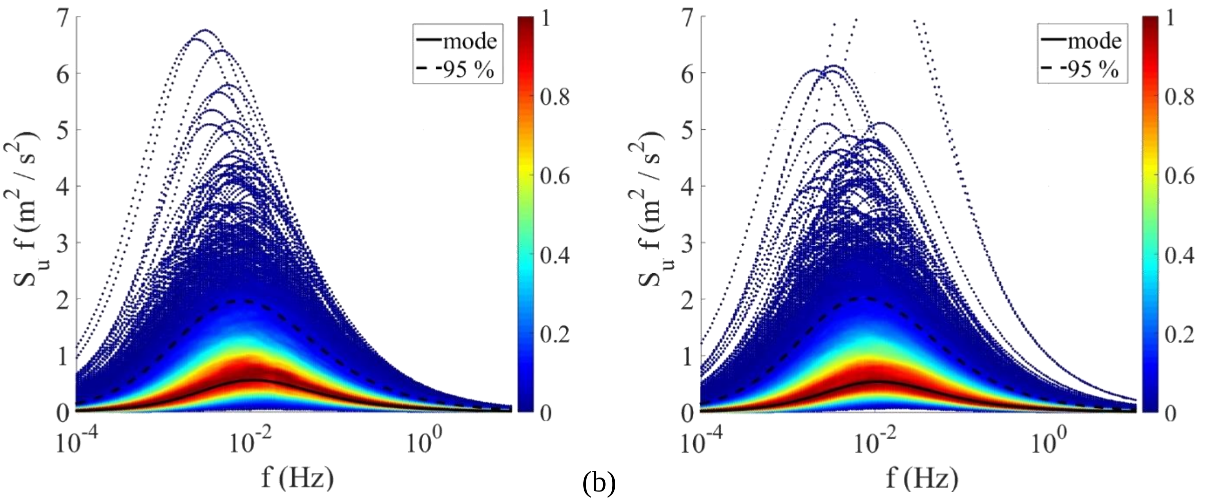

Fig. 19. Auto-spectral density of the along-wind turbulence: (a) measured and (b) simulated

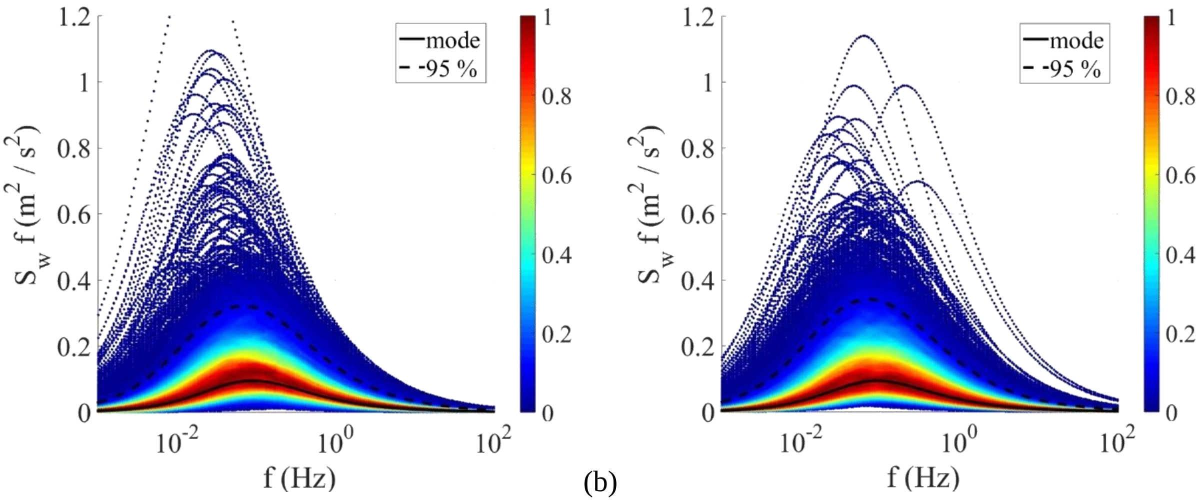

(a) (b)

Fig. 20. Auto-spectral density of the vertical turbulence: (a) measured and (b) simulated

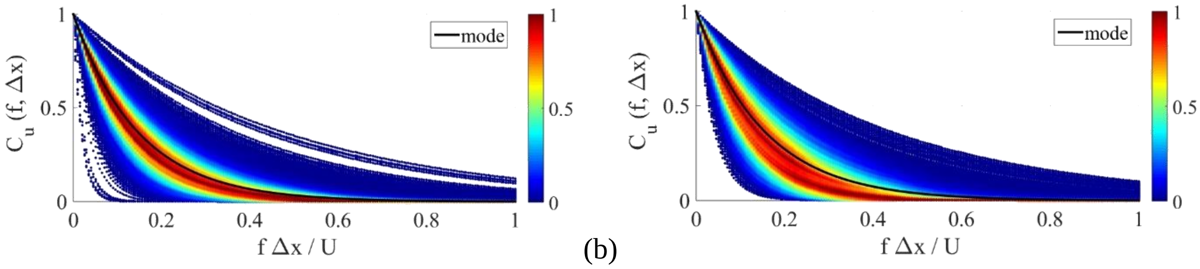

(a) (b)

Fig. 21. Normalized co-spectra of the along-wind turbulence: (a) measured and (b) simulated

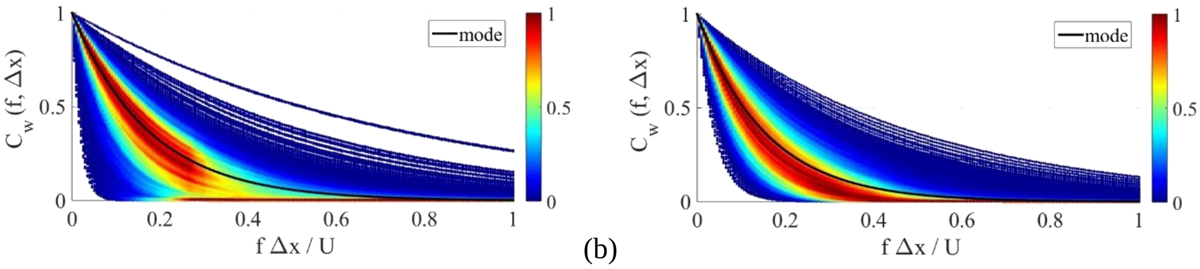

(a) (b)

Fig. 22. Normalized co-spectra of the vertical turbulence: (a) measured and (b) simulated

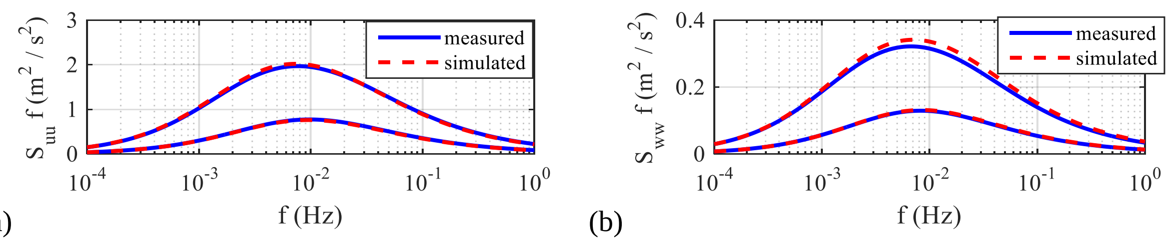

(a) (b)

Fig. 23. Comparison of measured and simulated auto-spectra: (a) along-wind and (b) vertical turbulence (the curves show 50 and 95 percentile values)

Unlike the auto-spectra, the normalized co-spectra do not follow a lognormal distribution, since it is simply the exponential of a lognormally distributed random variable. Therefore, the spectral density tensors for both turbulence components deviate from the lognormal distribution, when the separation distance is larger. Note that the amplitude of the spectra becomes rather small in that case. This result is illustrated in Fig. 24 and Fig. 25. by showing the probability distributions of the spectral tensors at few important natural frequencies of the HB. Those natural frequencies, obtained through finite element analysis (Fenerci and Øiseth, 2017), are listed in Table 7 with their associated mode shape.

Table 7 First few fundamental natural frequencies and mode shapes of the Hardanger Bridge

Mode	Frequency (Hz)	Period (seconds)	Description of the dominant motion
1	0.05	20.00	Symmetric lateral vibration of the deck
2	0.098	10.20	Asymmetric lateral vibration of the deck
3	0.11	9.09	Asymmetric vertical vibration of the deck
4	0.14	7.14	Symmetric vertical vibration of the deck
15	0.36	2.78	Symmetric torsional vibration of the deck

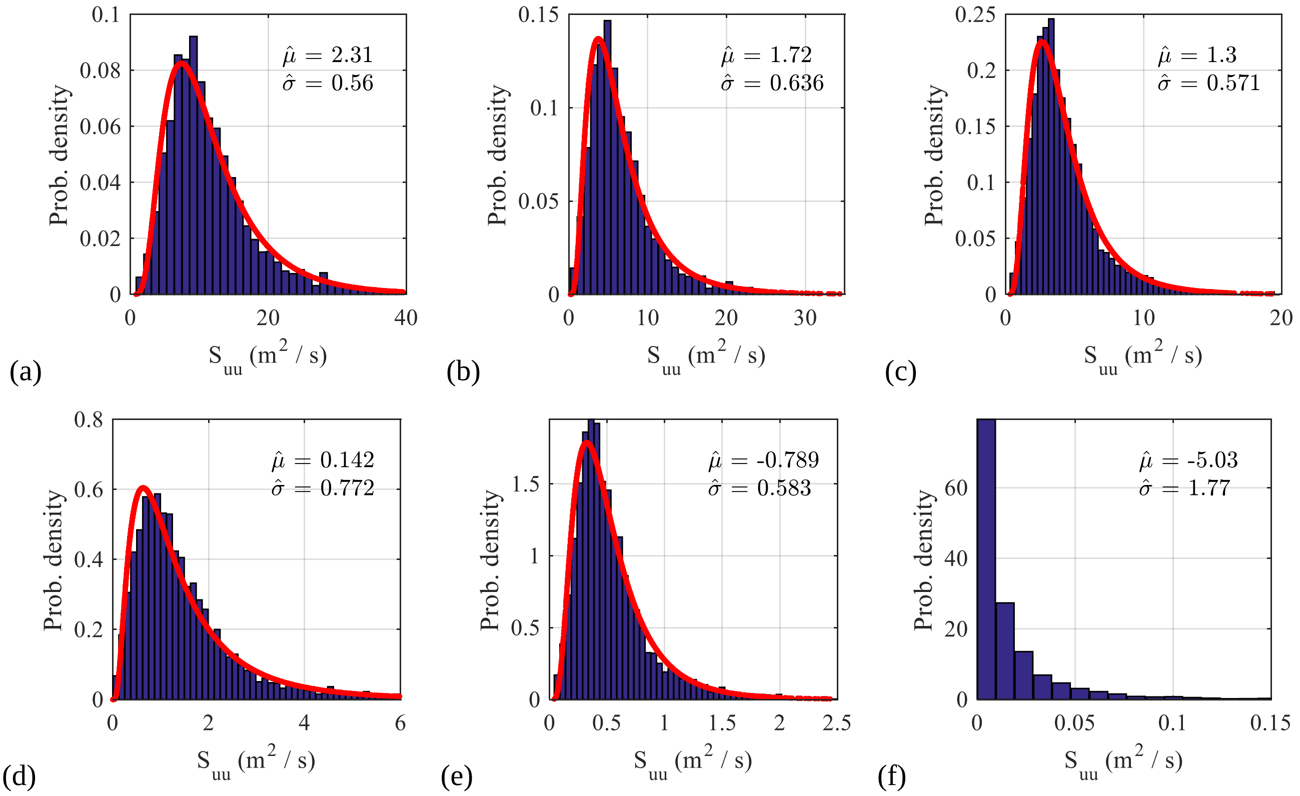

Fig. 24. Probability distributions of the spectral densities of the along-wind turbulence: (a) f = 0.05 Hz, Δx = 0 (b); f = 0.05 Hz, Δx = 20 m; (c) f = 0.098, Hz Δx = 0; (d) f = 0.098, Hz Δx = 20 m; (e) f = 0.36 Hz, Δx = 0 and (f) f = 0.36 Hz, Δx = 20 m (red curves show the lognormal fit)

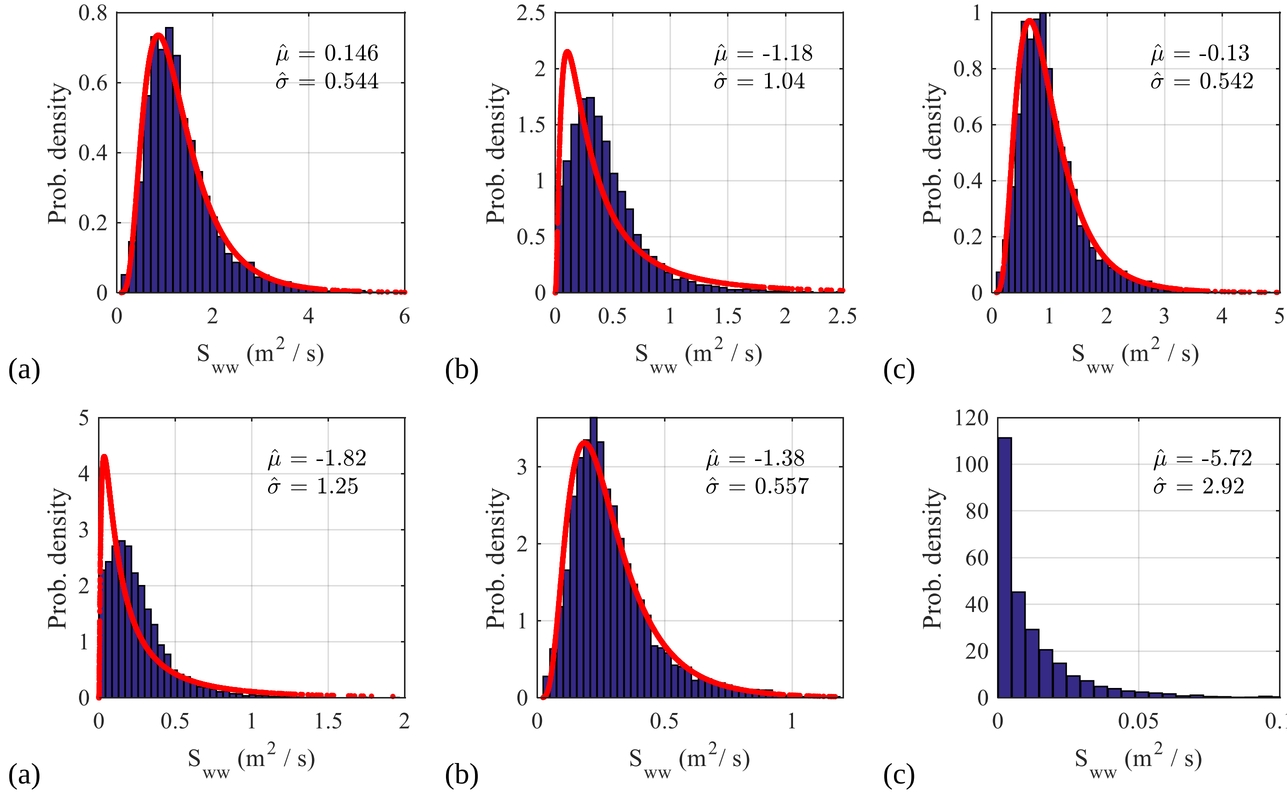

Fig. 25. Probability distributions of the spectral densities of the vertical turbulence: (a) f = 0.11 Hz, Δx = 0; (b) f = 0.11 Hz, Δx = 20 m; (c) f = 0.14 Hz, Δx = 0; (d) f = 0.14 Hz, Δx = 20 m; (e) f = 0.36 Hz, Δx = 0 and (f) f = 0.36 Hz, Δx = 20 m (red curves show the lognormal fit)

The probability distributions showed that it is possible to model the measured spectra with a lognormal distribution, at least for small separations. This allows further and more elaborate comparisons of the distributions of the measured and simulated spectral densities. To that extent, the correlation coefficients and lognormal distribution parameters were estimated for the measured and simulated spectral tensors and presented in Fig. 26 - Fig. 30 for the sake of comparison. A good overall agreement can be observed between the contour plots. Since it is difficult to observe the agreement in detail, especially for the important range of small separation distances and low frequencies, a numerical comparison is sought. For this purpose, surfaces were fitted to both data, where the coefficients were obtained through a least-squares approximation. The equations of the surfaces, the estimated coefficients and the R^2 values as a measure of the goodness of the fits, are presented in Table 8 for the correlation coefficients and in Table 9 for the lognormal distribution parameters. Finally, the measured and simulated spectral tensors were compared at few important natural frequencies of the bridge (Fig. 31 and Fig. 32). Excellent agreement is observed except for the parameter $\tilde{\sigma}_{S_{ww}}(f, \Delta x)$, where the discrepancy increases with increasing separation distance. In the important range of separation where the magnitude of the spectra is large, the discrepancy remains within a reasonable margin.

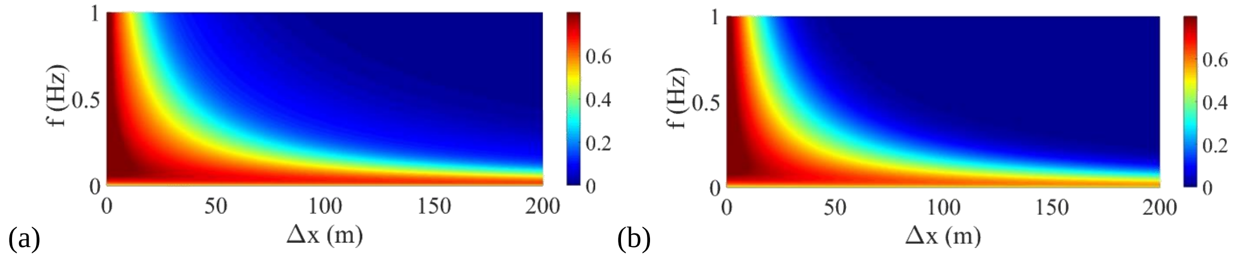

Fig. 26. Correlation coefficients $\rho_{S_{uu}S_{ww}}(f,\Delta x)$: (a) measured and (b) simulated

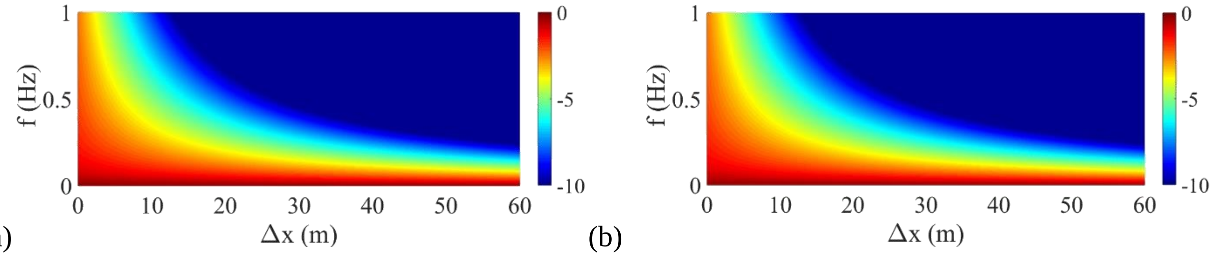

(a) (b)

Fig. 27. Parameters $\tilde{\mu}_{S_{uu}}(f,\Delta x)$: (a) measured and (b) simulated

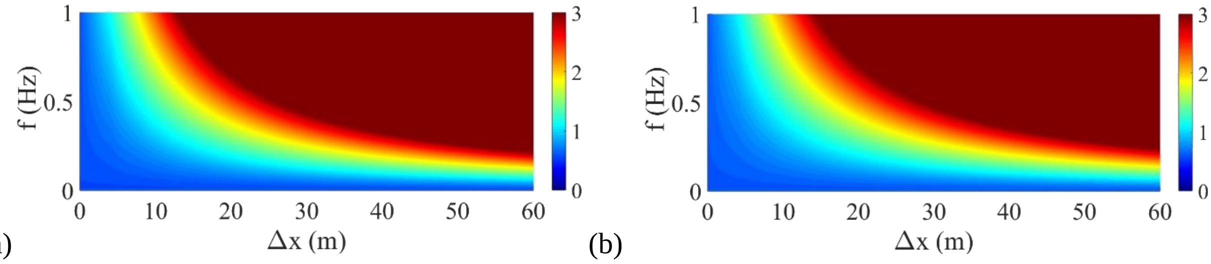

(a) (b)

Fig. 28. Parameters $\tilde{\sigma}_{S_{uu}}(f,\Delta x)$: (a) measured and (b) simulated

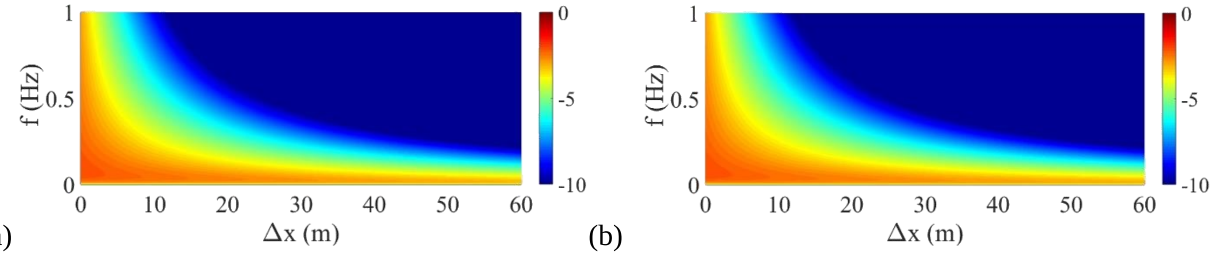

(a) (b)

Fig. 29. Parameters $\tilde{\mu}_{S_{ww}}(f,\Delta x)$: (a) measured and (b) simulated

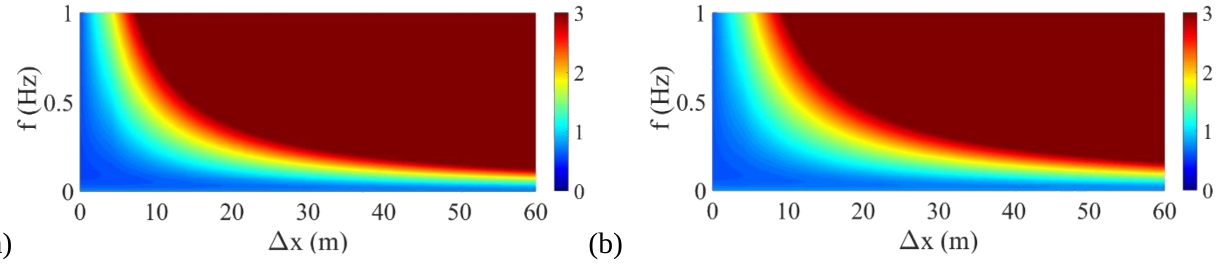

(a) (b)

Fig. 30. Parameters $\tilde{\sigma}_{S_{ww}}(f,\Delta x)$: (a) measured and (b) simulated

Table 8 Surface fit to the correlation coefficients of the along-wind and vertical spectra

surface equation	$\rho_{S_{uu}S_{ww}}(f,\Delta x) = p_0 + p_x f + p_y(\Delta x) + p_{xy} f(\Delta x) + p_{xx} f^2 + p_{yy}(\Delta x)^2$						
coefficients	p_0	p_x	p_y	p_{xy}	p_{xx}	p_{yy}	R^2
measured	1.126	-1.464	-0.00888	0.9121	0.000621	2.89E-05	0.87
simulated	1.08	-1.404	-0.00943	0.848	0.001138	3.11E-05	0.86

Table 9 Surface fits to the lognormal distribution parameters of the along-wind and vertical spectra

surface equation		$p_0 + p_x f + p_y(\Delta x) + p_{xy} f(\Delta x) + p_{xx} f^2 + p_{yy}(\Delta x)^2$			
parameter	coefficients	p_0	p_x	p_{xy}	R^2
$\tilde{\mu}_{S_{uu}}(f,\Delta x)$	measured	1.522	-4.751	-0.5886	0.999
	simulated	1.498	-4.754	-0.5992	0.999
$\tilde{\sigma}_{S_{uu}}(f,\Delta x)$	measured	0.2299	-0.03733	0.2183	0.999
	simulated	0.2179	-0.04053	0.2335	0.999
$\tilde{\mu}_{S_{ww}}(f,\Delta x)$	measured	0.3553	-3.852	-0.6029	0.999
	simulated	0.3973	-3.804	-0.6016	0.999
$\tilde{\sigma}_{S_{ww}}(f,\Delta x)$	measured	0.263	0.1371	0.3873	0.999
	simulated	0.2308	-0.01032	0.236	0.999

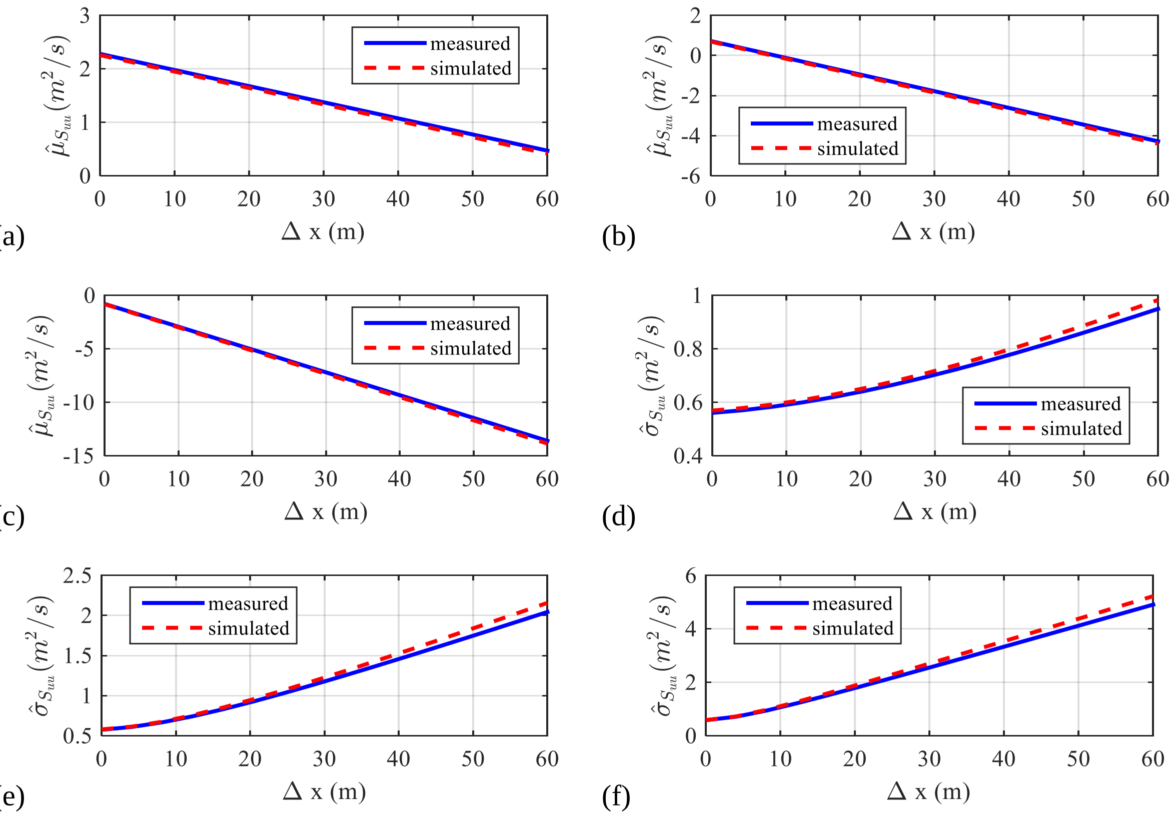

Fig. 31. Parameters for the spectral density of the along-wind turbulence: (a) f = 0.05 Hz; (b) f = 0.098 Hz; (c) f = 0.36 Hz; (d) f = 0.05 Hz; (e) f = 0.098 Hz and (f) f = 0.36 Hz

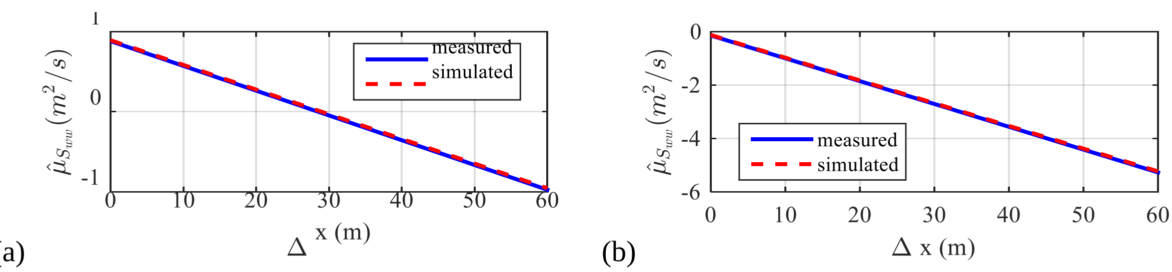

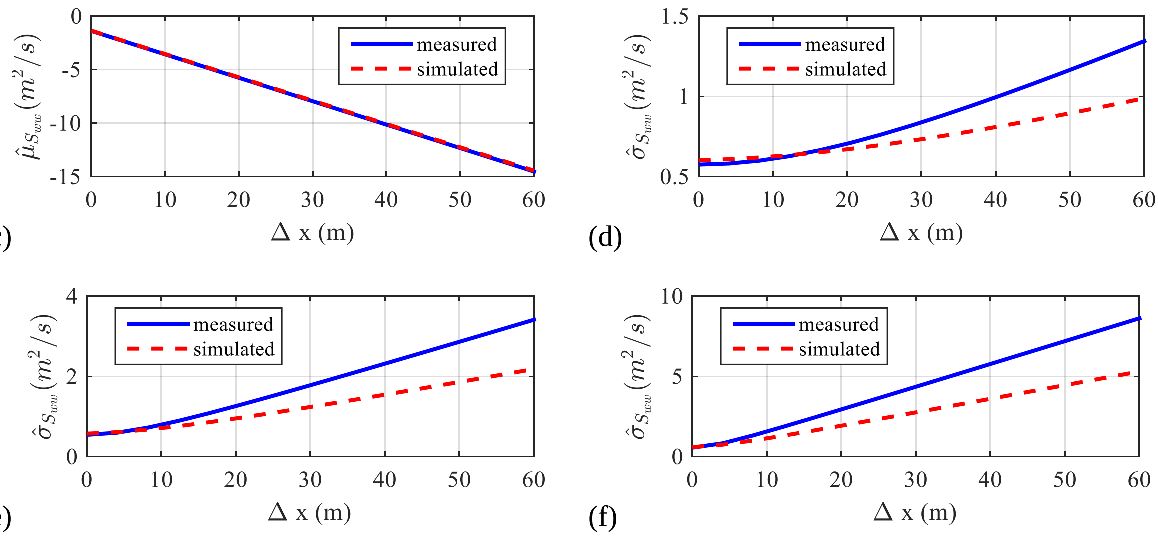

Fig. 32. Parameters for the spectral density of the vertical turbulence: (a) f = 0.11 Hz; (b) f = 0. 14 Hz; (c) f = 0.36 Hz; (d) f = 0.11 Hz; (e) f = 0. 14 Hz and (f) f = 0.36 Hz

Simulations for the design wind speed

Previous investigations provided a probabilistic model with good confidence in describing the variability and statistical properties of the turbulence field at the Hardanger Bridge site. Now, using the established model, simulations of the turbulence field can be conducted for the design wind speed of the bridge. The design wind speed of the HB for a 10-minute averaging interval, which is the short-term extreme wind speed for a 50-year return period (0.02 annual probability of exceedance), was provided as 39 m/s (Statens-Vegvesen, 2006). Given the design wind speed, 1000 wind turbulence fields were generated for the east and west directions separately. The first 10 simulations of the parameters are listed in Table 10. The resulting autospectra and normalized co-spectra are presented in Fig. 33 and Fig. 34, respectively. On the same plots, the design spectra are also indicated. It is seen that for the along-wind turbulence, the design spectra provides slightly higher values than the mode, where for the vertical turbulence it is on the higher side, closer to the 95th percentile. The design normalized co-spectra are also almost in the middle of the scatter. However, it is obvious that both spectra were exceeded by many of the simulations. Therefore, it can be stressed again that a deterministic description of the variable turbulence fields causes an oversimplification of the phenomenon, and it is not unexpected that this approach results into unconservative designs.

Table 10 First 10 simulations of the turbulence parameters for a design wind speed U = 39 m/s

Sim. No.	EAST						WEST					
	σ_u	σ_w	A_u	A_w	K_u	K_w	σ_u	σ_w	A_u	A_w	K_u	K_w
1	5.24	2.06	35.74	3.71	13.90	10.37	4.72	1.88	75.48	5.31	8.61	11.79
2	8.19	2.47	99.77	2.40	8.01	4.96	4.95	1.77	38.89	1.75	4.87	6.77
3	4.51	1.37	102.65	3.94	9.29	11.28	9.13	2.99	177.62	7.27	10.38	8.69
4	6.80	2.25	50.48	3.73	7.64	4.44	6.78	2.29	75.51	3.06	7.66	11.18
5	3.86	1.54	27.15	3.11	5.74	6.56	4.03	1.58	30.74	1.79	9.08	5.79
6	4.24	1.61	24.09	2.68	6.35	8.69	3.83	1.93	29.81	3.94	8.64	5.53
7	5.16	1.94	47.34	2.84	2.93	5.26	4.97	2.11	69.05	5.85	10.72	9.79
8	3.95	1.24	29.38	1.60	6.22	8.12	5.25	1.68	93.77	3.35	4.45	8.10
9	4.76	2.02	30.57	3.58	4.80	7.83	9.38	4.16	87.62	8.56	12.49	11.32

10	5.66	1.80	32.91	1.17	7.32	10.91	6.11	2.03	92.89	3.68	11.92	13.18

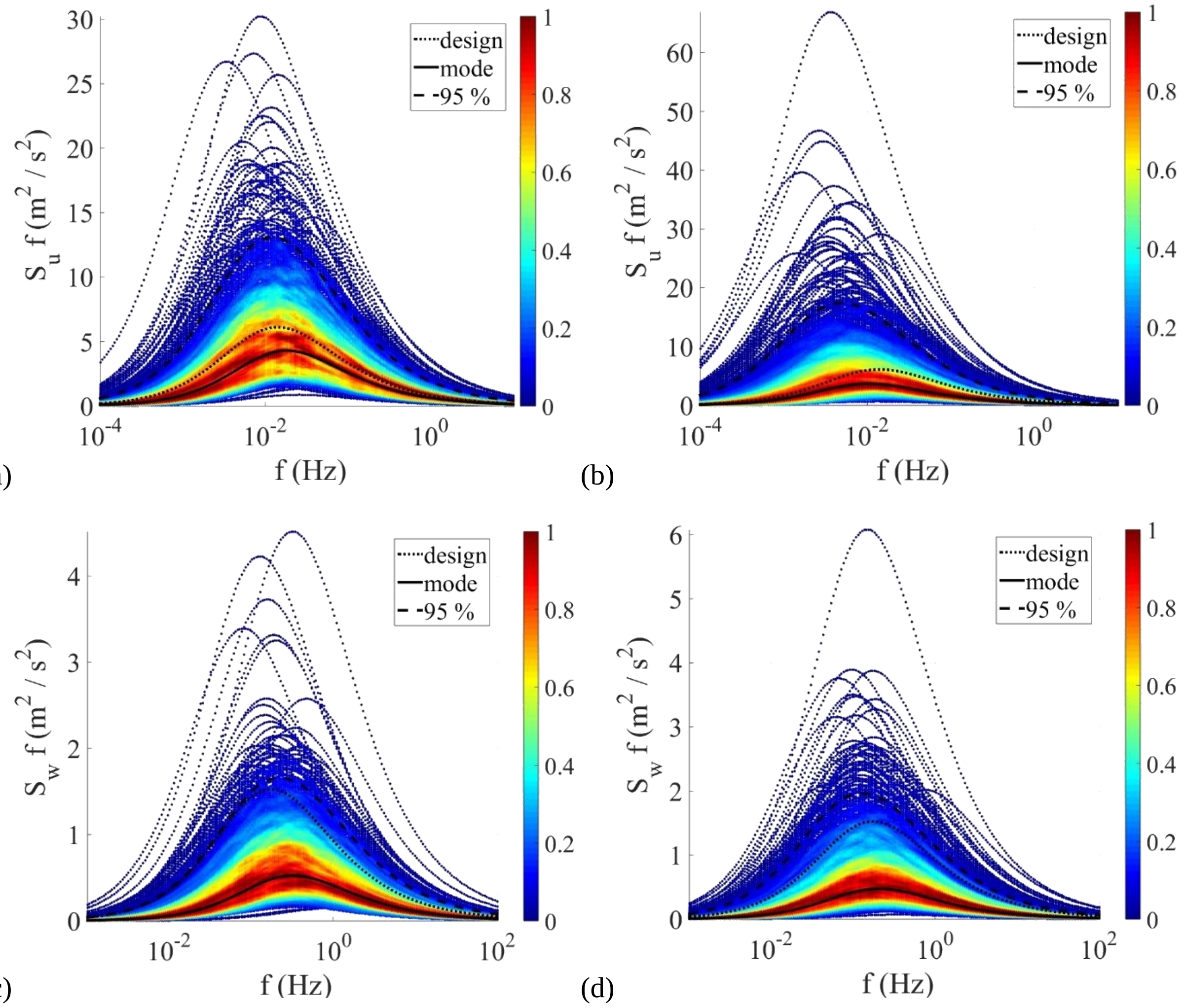

(a) (b)

(c) (d)

Fig. 33. Simulations of the autospectral density of the turbulence for a design wind speed of 39 m/s: the (a) along-wind turbulence for the easterly winds; (b) along-wind turbulence for the westerly winds; (c) vertical turbulence for the easterly winds and (d) vertical turbulence for the westerly winds (1000 simulations, the color bar shows the relative data density in the plotting area)

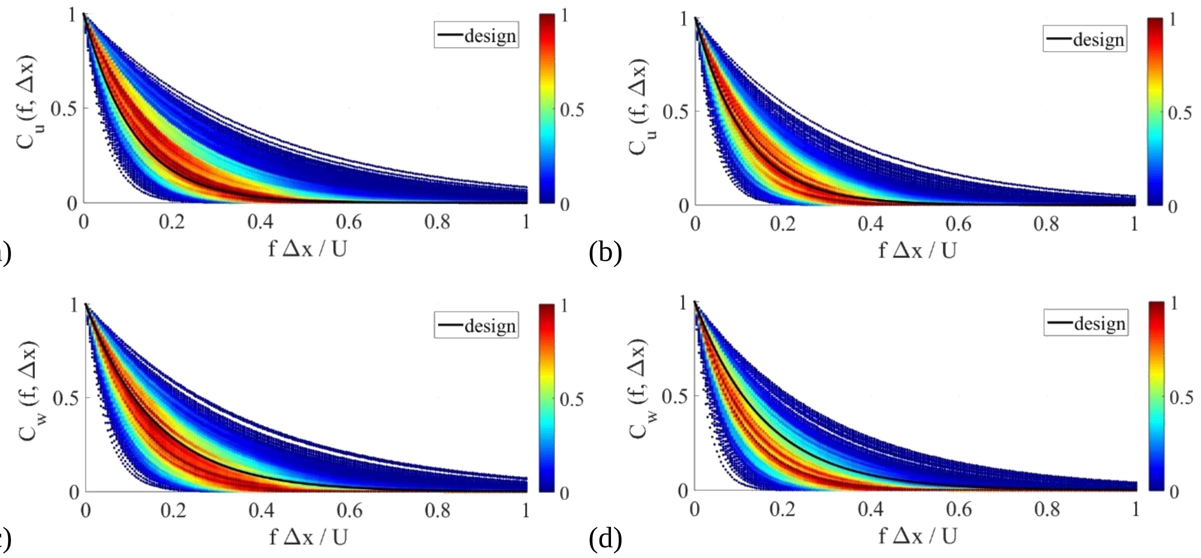

(a) (b)

(c) (d)

Fig. 34. Simulations of the normalized co-spectra of the turbulence for the design wind speed of 39 m/s: the (a) along-wind turbulence for the easterly winds; (b) along-wind turbulence for the westerly winds; (c) vertical turbulence for the easterly winds and (d) vertical turbulence for the westerly winds (1000 simulations, the color bar shows the relative data density in the plotting area)

Finally, as an illustrative and comparative exercise, simulations were conducted using a probabilistic model formulated by Solari and Piccardo (2001) almost two decades ago. In their study, the researchers adopted two simple parametric expressions for the autospectra and the normalized co-spectra. Neglecting the cross-spectral densities of the *u* and *w* components and discarding the *v* turbulence component as before, the spectra can be written as

$$\begin{aligned} \frac{S_{u,w} f}{\sigma_{u,w}{}^{2}} &= \frac{6.868\, fL_{u,w}/U}{\left(1+1.5(6.868)\, fL_{u,w}/U\right)^{5/3}} \\ C_{u,w} &= \exp\left(-K_{u,w}\frac{fz}{U}\right) \end{aligned} \tag{12}$$

where $L_{u,w}$ are the integral length scales of turbulence. The length scales and standard deviations of turbulence components are estimated through

$$\begin{aligned} \sigma_{u,w} &= \beta_{u,w} u_{*} \\ L_{u,w} &= 300\lambda_{u,w}(z/200)^{\upsilon} \\ \upsilon &= 0.67+0.05\ln(z_0) \end{aligned} \tag{13}$$

where u_{*} is the friction velocity and z_0 is the roughness length. Assuming that the coefficients $\beta_{u,w}$, $\lambda_{u,w}$ and $K_{u,w}$ are normally distributed random variables, Solari and Piccardo collected an extensive amount of measurement data from literature to obtain their first and second statistical moments. The resulting mean values and covariance matrices for the coefficients were given as

$$\begin{aligned} &\mu_{\beta} = \begin{bmatrix} 1 \\ 0.25 \end{bmatrix},\ \mathrm{cov}(\beta) = E\left[\beta_u\right]^2 \begin{bmatrix} 0.0625 & 0.0155 \\ 0.0155 & 0.0065 \end{bmatrix},\ E\left[\beta_u\right] = 6-1.1\arctan\left(\ln(z_0)+1.75\right) \\ &\mu_{\lambda} = \begin{bmatrix} 1 \\ 0.1 \end{bmatrix},\ \mathrm{cov}(\lambda) = \begin{bmatrix} 0.0625 & 0.006 \\ 0.006 & 0.0015 \end{bmatrix} \\ &\mu_{K} = \begin{bmatrix} 10 \\ 6.5 \end{bmatrix},\ \mathrm{cov}(K) = \begin{bmatrix} 16 & 5.2 \\ 5.2 & 6.76 \end{bmatrix} \end{aligned} \tag{14}$$

For the HB, z_0 can be taken as 0.01 m using the design basis (Statens-Vegvesen, 2006). The friction velocity is taken as 1.77 m/s following the ESDU 85020 (2001) guidelines. Using the above statistical properties, 1000 simulations of correlated normally distributed variables were obtained. Note that if the roughness coefficient can be defined for different directions, the model can account for the wind direction. Here, with the available design values, common spectra were obtained for all wind directions. The resulting simulated autospectra and normalized co-spectra are presented in Fig. 35. The design curves are also shown in the figures. Considering that the model is actually limited to a flat homogenous terrain and neutral atmospheric conditions, which is far from the conditions at the HB site, the simulated spectra do not provide results that are far off the measurements but rather present a more conservative version of the site-specific simulations, as shown in the figure. The overestimation of the along-wind turbulence spectra might be considered severe. It should also be noted that the model is quite sensitive to the friction velocity and the roughness coefficient. The scatter is also higher, which results from the use of Gaussian parameters rather than lognormal parameters. In summary, it seems that the model by Solari and Piccardo can be a good alternative in cases where no data are available. It is also likely that the model performs better in less complex terrain, given that the friction velocity is estimated correctly. More investigations that use data from such sites are needed.

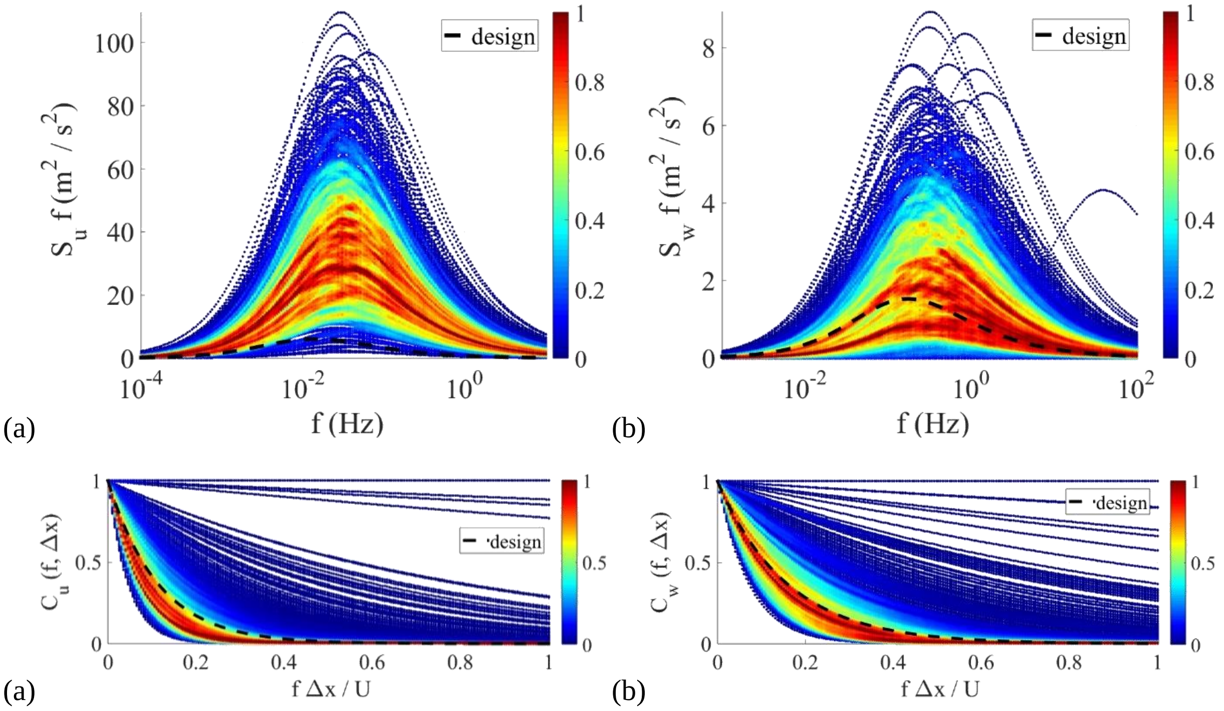

Fig. 35. Simulations of the autospectra and normalized co-spectra of the turbulence for the design wind speed using Solari and Piccardo's probabilistic model: the (a) autospectral density of the along-wind turbulence; (b) autospectral density of the vertical turbulence; (c) normalized co-spectra of the along-wind turbulence and (d) normalized co-spectra of the vertical turbulence

Concluding Remarks

The turbulence field along the single span of the Hardanger Bridge was modeled here in a probabilistic manner using the lognormal distribution coefficients and correlation coefficients of the turbulence parameters, which were obtained from an analysis of the long-term monitoring data. The following conclusions were reached for the specific case considered:

- For a 10-minute averaging interval, neglecting the cross-wind turbulence and cross-spectral density of the *u*-*w* turbulence, the wind field along the structure was defined by just six parameters, which were then treated as random variables.
- Conditional on the mean wind speed and direction, the turbulence parameters followed a lognormal distribution.
- Detailed comparisons between the simulations of the turbulence parameters and the corresponding turbulence spectra with the measurement data provided confidence in the probabilistic model in representing the site-specific variability.
- As noted in the paper, the model is suitable for use in reliability-based or performance-based frameworks or long-term extreme response predictions. The probabilistic model also allows assessment of the propagation of turbulence related uncertainties into the response prediction.

- Using the available data on wind characteristics, such a model can easily be devised at the design stage of such long-span bridges when the terrain-induced randomness in the wind field is considered significant.

Acknowledgements

The research described in this paper was financially supported by the Norwegian Public Roads Administration as part of the Ferry-Free Coastal E39 project. The authors appreciate this support.

References

Bastos, F., Caetano, E., Cunha, Á., Cespedes, X., Flamand, O., 2018. Characterisation of the wind properties in the Grande Ravine viaduct. J. Wind Eng. Ind. Aerodyn. 173, 112–131. doi:10.1016/j.jweia.2017.12.012

Busch, N.E., Panofsky, H.A., 1968. Recent spectra of atmospheric turbulence. Q. J. R. Meteorol. Soc. 94, 132–148. doi:10.1002/qj.49709440003

Cao, S., Tamura, Y., Kikuchi, N., Saito, M., Nakayama, I., Matsuzaki, Y., 2009. Wind characteristics of a strong typhoon. J. Wind Eng. Ind. Aerodyn. 97, 11–21. doi:10.1016/j.jweia.2008.10.002

Caracoglia, L., Jones, N.P., 2009. Analysis of full-scale wind and pressure measurements on a low-rise building. J. Wind Eng. Ind. Aerodyn. 97, 157–173. doi:10.1016/j.jweia.2009.06.001

Cheynet, E., 2016. Wind-induced vibrations of a suspension bridge. Univ. Stavanger.

Cheynet, E., Jakobsen, J.B., Snæbjørnsson, J., 2016. Buffeting response of a suspension bridge in complex terrain. Eng. Struct. 128, 474–487. doi:10.1016/j.engstruct.2016.09.060

Ciampoli, M., Petrini, F., Augusti, G., 2011. Performance-Based Wind Engineering: Towards a general procedure. Struct. Saf. 33, 367–378. doi:https://doi.org/10.1016/j.strusafe.2011.07.001

Cross, E.J., Koo, K.Y., Brownjohn, J.M.W., Worden, K., 2013. Long-term monitoring and data analysis of the Tamar Bridge. Mech. Syst. Signal Process. 35, 16–34. doi:10.1016/j.ymssp.2012.08.026

Davenport, A.G., 1983a. The relationship of reliability to wind loading. J. Wind Eng. Ind. Aerodyn. 13, 3–27. doi:https://doi.org/10.1016/0167-6105(83)90125-3

Davenport, A.G., 1983b. On the assessment of the reliability of wind loading on low buildings. J. Wind Eng. Ind. Aerodyn. 11, 21–37. doi:https://doi.org/10.1016/0167-6105(83)90088-0

Davenport, A.G., 1962. Buffeting of a suspension bridge by storm winds. J. Struct. Div. 88, 233–268. doi:10.4319/lo.2013.58.2.0489

Davenport, A.G., 1961. The spectrum of horizontal gustiness near the ground in high winds. Q. J. R. Meteorol. Soc. 87, 194–211. doi:10.1002/qj.49708737208

Dunham, K.K., 2016. Coastal Highway Route E39 - Extreme Crossings, in: Transportation Research Procedia. pp. 494–498. doi:10.1016/j.trpro.2016.05.102

Ellevset, O., Skorpa, L., 2011. A feasibility study – How to cross the wide and deep Sognefjord, summary. Norwegian Public Roads Administration - Western Region Projects Division, Norway.

ESDU 086010, 2001. Characteristics of atmospheric turbulence near the ground Part 3: variations in space and time for strong winds (neutral atmosphere), 2008th ed. ESDU International plc, London.

ESDU 85020, 2001. Characteristics of atmospheric turbulence near groud Part 2: signle point data for strong winds (neutral atmosphere). ESDU International plc, London.

Fenerci, A., Øiseth, O., 2018. Strong wind characteristics and dynamic response of a long-span suspension bridge during a storm. J. Wind Eng. Ind. Aerodyn. 172, 116–138.

Fenerci, A., Øiseth, O., 2017. Measured Buffeting Response of a Long-Span Suspension Bridge Compared with Numerical Predictions Based on Design Wind Spectra. J. Struct. Eng. (United States) 143. doi:10.1061/(ASCE)ST.1943-541X.0001873

Fenerci, A., Øiseth, O., Rønnquist, A., 2017. Long-term monitoring of wind field characteristics and dynamic response of a long-span suspension bridge in complex terrain. Eng. Struct. 147, 269–284. doi:10.1016/j.engstruct.2017.05.070

Giske, F.-I.G., Leira, B.J., Øiseth, O., 2017. Full long-term extreme response analysis of marine structures using inverse FORM. Probabilistic Eng. Mech. 50, 1–8. doi:https://doi.org/10.1016/j.probengmech.2017.10.007

Höbbel, T., Thiele, K., Clobes, M., 2018. Wind turbulence parameters from three dimensional full-scale measurements at 344 m high guyed mast site Gartow 2. J. Wind Eng. Ind. Aerodyn. 172, 341–350. doi:10.1016/j.jweia.2017.11.001

Hui, M.C.H., Larsen, A., Xiang, H.F., 2009a. Wind turbulence characteristics study at the Stonecutters Bridge site: Part II: Wind power spectra, integral length scales and coherences. J. Wind Eng. Ind. Aerodyn. 97, 48–59. doi:10.1016/j.jweia.2008.11.003

Hui, M.C.H., Larsen, A., Xiang, H.F., 2009b. Wind turbulence characteristics study at the Stonecutters Bridge site: Part I-Mean wind and turbulence intensities. J. Wind Eng. Ind. Aerodyn. 97, 22–36. doi:10.1016/j.jweia.2008.11.002

Jain, A., Jones, N.P., Scanlan, R.H., 1996. Coupled Flutter and Buffeting Analysis of Long-Span Bridges. J. Struct. Eng. 122, 716–725. doi:10.1061/(ASCE)0733-9445(1996)122:7(716)

Kaimal, J.C.J., Wyngaard, J.C.J., Izumi, Y., Coté, O.R., Cote, O.R., 1972. Spectral Characteristics of Surface-Layer Turbulence. Q. J. … 98, 563–589. doi:10.1002/qj.49709841707

Kareem, A., 1988. Aerodynamic response of structures with parametric uncertainties. Struct. Saf. 5, 205–225. doi:10.1016/0167-4730(88)90010-0

Kareem, A., 1987. Wind effects on structures: a probabilistic viewpoint. Probabilistic Eng. Mech. 2, 166–200. doi:10.1016/0266-8920(87)90009-9

Krenk, S., 1996. Wind Field Coherence And Dynamic Wind Forces, in: Naess, A., Krenk, S. (Eds.), IUTAM Symposium on Advances in Nonlinear Stochastic Mechanics: Proceedings of the IUTAM Symposium Held in Trondheim, Norway, 3--7 July 1995. Springer Netherlands, Dordrecht, pp. 269–278. doi:10.1007/978-94-009-0321-0_25

Kristensen, L., Jensen, N.O., 1979. Lateral coherence in isotropic turbulence and in the natural wind. Boundary-Layer Meteorol. 17, 353–373. doi:10.1007/BF00117924

Li, L., Kareem, A., Xiao, Y., Song, L., Zhou, C., 2015. A comparative study of field measurements of the turbulence characteristics of typhoon and hurricane winds. J. Wind Eng. Ind. Aerodyn. 140. doi:10.1016/j.jweia.2014.12.008

Liu, Z., Prevatt, D.O., Aponte-Bermudez, L.D., Gurley, K.R., Reinhold, T.A., Akins, R.E., 2009. Field measurement and wind tunnel simulation of hurricane wind loads on a single family dwelling. Eng. Struct. 31, 2265–2274. doi:10.1016/j.engstruct.2009.04.009

Mann, J., 2006. The spatial structure of neutral atmospheric surface-layer turbulence. J. Fluid Mech. 273, 141. doi:10.1017/S0022112094001886

Mann, J., 2000. The spectral velocity tensor in moderately complex terrain. J. Wind Eng. Ind. Aerodyn. 88, 153–169. doi:https://doi.org/10.1016/S0167-6105(00)00046-5

Minciarelli, F., Gioffrè, M., Grigoriu, M., Simiu, E., 2001. Estimates of extreme wind effects and wind load factors: influence of knowledge uncertainties. Probabilistic Eng. Mech. 16, 331–340. doi:https://doi.org/10.1016/S0266-8920(01)00024-8

Miyata, T., Yamada, H., Katsuchi, H., Kitagawa, M., 2002. Full-scale measurement of Akashi-Kaikyo Bridge during typhoon. J. Wind Eng. Ind. Aerodyn. 90, 1517–1527. doi:10.1016/S0167-6105(02)00267-2

Naess, A., Moan, T., 2012. Stochastic Dynamics of Marine Structures. Cambridge University Press, Cambridge. doi:DOI: 10.1017/CBO9781139021364

Nielsen, M., Larsen, G.C., Hansen, K.S., 2007. Simulation of inhomogeneous, non-stationary and non-Gaussian turbulent winds, in: Journal of Physics: Conference Series. doi:10.1088/1742-6596/75/1/012060

Øiseth, O., Rönnquist, A., Sigbjörnsson, R., 2013. Effects of co-spectral densities of atmospheric turbulence on the dynamic response of cable-supported bridges: A case study. J. Wind Eng. Ind. Aerodyn. 116, 83–93. doi:10.1016/j.jweia.2013.03.001

Pagnini, L., 2010. Reliability analysis of wind-excited structures. J. Wind Eng. Ind. Aerodyn. 98, 1–9. doi:https://doi.org/10.1016/j.jweia.2009.08.010

Panofsky, H.A., Larko, D., Lipschutz, R., Stone, G., Bradley, E.F., Bowen, A.J., H??jstrup, J., 1982. Spectra of velocity components over complex terrain. Q. J. R. Meteorol. Soc. 108, 215–230. doi:10.1002/qj.49710845513

Scanlan, R.H., 1978. The action of flexible bridges under wind, II: Buffeting theory. J. Sound Vib. 60, 187–199. doi:10.1016/S0022-460X(78)80029-7

Simiu, E., Scanlan, R.H., 1996. Winds Effects on Structures: Fundamentals and Applications to Design, 3rd ed. Wiley.

Solari, G., 1997. Wind-excited response of structures with uncertain parameters. Probabilistic Eng. Mech. 12, 75–87. doi:10.1016/S0266-8920(96)00027-6

Solari, G., 1987. Turbulence Modeling for Gust Loading. J. Struct. Eng. 113, 1550–1569. doi:10.1061/(ASCE)0733-9445(1987)113:7(1550)

Solari, G., Piccardo, G., 2001. Probabilistic 3-D turbulence modeling for gust buffeting of structures. Probabilistic Eng. Mech. 16, 73–86. doi:10.1016/S0266-8920(00)00010-2

Spence, S.M.J., Kareem, A., 2014. Performance-based design and optimization of uncertain wind-excited dynamic building systems. Eng. Struct. 78, 133–144. doi:https://doi.org/10.1016/j.engstruct.2014.07.026

Statens-Vegvesen, 2006. The Hardanger Bridge design basis - wind characteristics.

The Mathworks Inc., 2015. MATLAB (R2015a). MathWorks Inc. doi:10.1007/s10766-008-0082-5

Tieleman, H.W., 1995. Universality of velocity spectra. J. Wind Eng. Ind. Aerodyn. 56, 55–69. doi:10.1016/0167-6105(94)00011-2

Tieleman, H.W., 1992. Wind characteristics in the surface layer over heterogeneous terrain. J. Wind Eng. Ind. Aerodyn. 41, 329–340. doi:10.1016/0167-6105(92)90427-C

Toriumi, R., Katsuchi, H., Furuya, N., 2000. A study on spatial correlation of natural wind. J. Wind Eng. Ind. Aerodyn. 87, 203–216. doi:10.1016/S0167-6105(00)00037-4

von Karman, T., 1948. Progress in the statistical theory of turbulence. Proc. Natl. Acad. Sci. U. S. A. 34, 530–539. doi:10.1073/pnas.34.11.530

Wang, H., Li, A., Niu, J., Zong, Z., Li, J., 2013. Long-term monitoring of wind characteristics at Sutong Bridge site. J. Wind Eng. Ind. Aerodyn. 115. doi:10.1016/j.jweia.2013.01.006

Welch, P.D., 1967. The Use of Fast Fourier Transform for the Estimation of Power Spectra: A Method Based on Time Averaging Over Short, Modified Periodograms. IEEE Trans. Audio Electroacoust. 15, 70–73. doi:10.1109/TAU.1967.1161901

Xu, Y.-L., 2013. Wind Effects on Cable-Supported Bridges. John Wiley & Sons.

Xu, Y., Øiseth, O., Naess, A., Moan, T., 2017. Prediction of long-term extreme load effects due to wind for cable-supported bridges using time-domain simulations. Eng. Struct. 148, 239–253. doi:10.1016/j.engstruct.2017.06.051

Zerovnik, G., Trkov, A., Kodeli, I.A., 2012. Correlated random sampling for multivariate normal and log-normal distributions. Nucl. Instruments Methods Phys. Res. Sect. A Accel. Spectrometers, Detect. Assoc. Equip. 690, 75–78. doi:10.1016/j.nima.2012.06.036

Zhang, L., Li, J., Peng, Y., 2008. Dynamic response and reliability analysis of tall buildings subject to wind loading. J. Wind Eng. Ind. Aerodyn. 96, 25–40. doi:https://doi.org/10.1016/j.jweia.2007.03.001